

# NATURE OR NURTURE? COLLISIONLESS EVOLUTION OF GALACTIC DISC-HALO SYSTEMS

by

J S BAUER

A thesis submitted to the  
Department of Physics  
in conformity with the requirements for  
the degree of Doctor of Philosophy

Queen's University  
Kingston, Ontario, Canada

October 2018

Copyright © J S Bauer, 2018

# Abstract

This is my abstract.

## Acknowledgments

Blah blah blah.

## Statement of Originality

Only required by CHEM, COMPUTING, GEOL, MATH and Physics (Ph.D. ONLY!).

# Contents

<b>Abstract</b>	<b>i</b>
<b>Acknowledgments</b>	<b>ii</b>
<b>Statement of Originality</b>	<b>iii</b>
<b>Contents</b>	<b>iv</b>
<b>List of Tables</b>	<b>vii</b>
<b>List of Figures</b>	<b>ix</b>
<b>Chapter 1: Introduction</b>	<b>1</b>
1.1 Section . . . . .	1
1.1.1 SubSection . . . . .	1
1.2 Motivation . . . . .	1
1.3 Problem . . . . .	1
1.4 Objective . . . . .	1
1.4.1 Hypothesis . . . . .	2
1.5 Contributions . . . . .	2
1.6 Organization of Thesis . . . . .	2
<b>Chapter 2: A Dynamical Recipe for Cosmological Disks</b>	<b>3</b>
2.1 Physical Motivation of Modeling . . . . .	4
2.2 Time Evolution of Collisionless Systems . . . . .	4
2.2.1 The Collisionless Boltzmann Equation . . . . .	4
2.2.2 Numerical Solutions . . . . .	4
2.3 Phase Space, Equilibrium, and Initial Conditions . . . . .	4
2.3.1 Jeans Modeling . . . . .	4
2.3.2 DF-based Models and the Strong Jeans Theorem . . . . .	4
2.3.3 Action-Angle Variables . . . . .	4
2.3.4 DFs as Functions of Actions . . . . .	4

2.4	Simulation Analysis: Paradigms and Tools . . . . .	4
2.4.1	WKB Wave Analysis . . . . .	4
2.4.2	Time Series Filtering . . . . .	4
2.4.3	MCMC . . . . .	4
2.5	Cosmology and Implications for Galaxy Studies . . . . .	4
2.5.1	Basic FRW Cosmology . . . . .	4
2.5.2	Extension of Numerical Methods . . . . .	4
2.5.3	Sampling Initial Conditions for Cosmological Simulations . . . . .	4
2.5.4	Cosmological Substructure and Halo Triaxiality . . . . .	4
2.5.5	Identifying Substructure in Simulations . . . . .	4
<b>Chapter 3:</b>	<b>A Method for Studying Discs in Cosmological Haloes</b>	<b>5</b>
3.1	Abstract . . . . .	5
3.2	Introduction . . . . .	6
3.3	Inserting a Stellar Disc into a Cosmological Halo . . . . .	12
3.3.1	Overview of Simulation Set . . . . .	12
3.3.2	Summary of Live Disc Insertion Scheme . . . . .	14
3.3.3	Halo Potential . . . . .	16
3.3.4	Disc DFs . . . . .	16
3.3.5	Rigid Disc Dynamics . . . . .	17
3.3.6	Test-bed Simulation of an Isolated Galaxy . . . . .	19
3.4	Cosmological Simulations . . . . .	22
3.4.1	Bar Formation . . . . .	28
3.4.2	Kicked-up Stars and Disc Heating . . . . .	29
3.5	Halo Substructure in the Presence of a Disc . . . . .	31
3.5.1	Global Properties of the Halo . . . . .	31
3.5.2	Subhalo Populations . . . . .	33
3.5.3	Case Study: A Sagittarius-like Dwarf . . . . .	37
3.6	Conclusions . . . . .	39
<b>Chapter 4:</b>	<b>Cosmological Bar Formation: Nature vs Nurture</b>	<b>49</b>
4.1	Abstract . . . . .	49
4.2	Introduction . . . . .	50
4.3	Theoretical Considerations . . . . .	56
4.3.1	$Q$ and $X$ . . . . .	56
4.3.2	Vertical Structure of Stellar Discs . . . . .	67
4.3.3	Effect of Gravitational Softening . . . . .	68
4.4	Models and Simulations . . . . .	70
4.4.1	Initial Conditions for Isolated Galaxy Simulations . . . . .	70
4.4.2	Description of simulations . . . . .	71

4.4.3	Comparison with Previous Work . . . . .	72
4.5	Isolated Galaxy Simulations . . . . .	74
4.5.1	Morphology of Bar Forming Galaxies . . . . .	74
4.5.2	Bar Strength Parameter $A_2$ . . . . .	74
4.5.3	Vertical Structure and Velocity Dispersion . . . . .	77
4.5.4	Simulations Where Buckling is Suppressed . . . . .	79
4.6	Cosmological Simulations . . . . .	80
4.6.1	Simulation Setup; Inserting Discs into Cosmological Haloes . .	81
4.6.2	Results . . . . .	84
4.7	Conclusions . . . . .	87
<b>Chapter 5: Summary and Conclusions</b>		<b>99</b>
5.1	Summary . . . . .	99
5.2	Future Work . . . . .	99
5.3	Conclusion . . . . .	99
<b>Chapter A: Euler's Equations in Comoving Coordinates</b>		<b>100</b>

# List of Tables

3.1	A summary of the simulation parameters, as discussed in the text. $M_d$ is the final disk mass, $R_{d,0}$ is the final disk scale radius, $N_d$ is the number of particles used to simulate the disk, $z_g$ and $z_l$ are the redshifts when the disk beings to grow and when it becomes live (respectively), $N_r$ is the effective resolution in the zoom-in region, and $L_{box}$ is the comoving size of the box. . . . .	11
-----	--	----



4.1	Summary of parameters for the simulations considered in this paper, the disk-halo simulations considered in Yurin and Springel (2015) (labeled YS15) and the Gauthier et al. (2006) (G06). $M_d$ is the final disc mass in units of $10^{10} M_\odot$ , $R_d$ is the disc scale radius in units of kpc, and $V_c$ and $\sigma_R$ are the circular speed and radial velocity dispersion in units of $\text{km s}^{-1}$ and evaluated at $R_p = 2.2R_d$ . For the disc aspect ratio, we quote $z_d/R_d$ where $z_d$ is the $\text{sech}^2$ -scale length. The velocity dispersion ratio $\sigma_R/\sigma_z$ , the $X$ and $Q$ parameters, the ratio of the halo density in the midplane to that of the disc, and the logarithmic derivative of the circular speed are also measured at $R_p$ . Finally, the softening length $\epsilon$ is given in units of kpc. Simulations A.III and B.III are the same as A.I and B.I except that they are run with vertical motions isotropized so as to shut off the buckling instability. . . . .	58
-----	--	----

# List of Figures

- 3.1 Kinematic variables for the rigid and live discs in an isolated, flattened halo as a function of time. The upper two panels show the Euler angles  $\theta$  and  $\phi$  for the rigid disc (dashed curves) and live disc (solid curves) where the live disc is introduced at  $t = 1$  Gyr (red vertical line). The bottom two panels show the  $x$  and  $y$  components of the angular velocity, as measured in the body coordinate system. In these two panels the solid curves show the  $\delta t \sim 150$  My moving average, which is used to initialize the live disc. . . . . 21
- 3.2 Face-on projections of the particle distribution for two snapshots of a live disc in a flattened halo. The solid line for scale is 25 kpc with a centre coincident with the disc's. . . . . 22
- 3.3 Surface density, vertical velocity dispersion, and scale height profiles as a function of Galactocentric radius  $R$  for 10 snapshots equally spaced in time. The top panel shows the surface density  $\Sigma(R)$  divided by  $\Sigma_0(R) = (M_d/2\pi R_d^2) \exp[-(R/R_d)]$  in order to highlight departures from a pure exponential disc. Likewise, in the middle panel, we show the ratio  $\sigma_z(R)/\sigma_{z,0}(R)$  where  $\sigma_{z,0} = \exp(-R/2R_d)$ . The bottom panel shows the RMS  $z$  as a function of  $R$ . . . . . 23

3.4	Kinematic variables for the rigid and live discs in our cosmological halo as a function of scale factor $a$ . Line types are the same as in Fig. 3.1. The live disc is introduced at a redshift $z = 1$ when the scale factor is $a = 0.5$ (red vertical line). The blue line shows the $\delta a \sim 0.04$ moving average calculated by averaging the last 300 points in the disc integration routine. . . . .	24
3.5	Circular speed curve decompositions at $z = 1$ (top row) and $z = 0$ (bottom row) for (from left to right) our LD, RD, and MN simulations. Halo contributions are represented as dot-dashed lines, disc contributions are represented by dashed lines, and the total rotation curve is given by a solid line. For reference, we have included the circular speed curve for the DMO halo (dot-dashed curve). . . . .	25
3.6	Projected density along three orthogonal directions for the live disc at four epochs between $z = 1$ and $z = 0$ . The projections are presented in physical units. The solid line for scale is 37 kpc with a centre coincident with the disc's. . . . .	27
3.7	Surface density, vertical velocity dispersion, and scale height profiles of the live disc for 10 snapshots equally spaced in scale factor $a$ between $a = 0.5$ ( $z = 1$ ) and $a = 1$ (present epoch). Panels are the same as in Fig. 3.3. . . . .	30
3.8	The ratio of halo density to the DMO simulation for MN (green), FO (teal), RD (red), and LD (purple) at $z = 1$ (dashed) and $z = 0$ (solid). The presence of the disc significantly increases the central concentration of the halo. . . . .	32

3.9	Axis ratios as a function of radius. Shown are the minor-to-major axis ratio (top panel) and the intermediate-to-major axis ratio (bottom panel) at $z = 1$ (dashed curves) and $z = 0$ (solid curves). Blue corresponds to DMO, green to MN, teal to FO, red to RD, and purple to LD. . . . .	34
3.10	Cumulative mass in subhaloes inside a radius $r$ (upper panel) and cumulative number of subhaloes (lower panel). We consider only subhaloes within 500 kpc of the halo centre and with a mass above $10^{7.5} M_{\odot}$ . The curves are blue (DMO), green (MN), teal (FO), red (RD), and purple (LD). . . . .	35
3.11	Differential mass distribution multiplied by $M^{0.9}$ for subhaloes above $10^{7.5} M_{\odot}$ . We make an outer radius cut at 500 kpc. The curves are blue (DMO), green (MN), teal (FO), red (RD), and purple (LD). . .	36
3.12	X-Y projections for a selected Sagittarius-like dwarf galaxy. The rows from top to bottom are no disc, a fixed Miyamoto-Nagai disc, a rigid disc, and a live disc. The scale factors in columns from left to right are 0.5, 0.55, 0.6, 0.65, and 0.7. The frame edges are 295 kpc on each side.	38
4.1	Rotation curve decomposition for our models. Total rotation curves are shown as solid lines while the separate contributions from the disc and halo are shown as dashed and dot-dashed curves, respectively. Blue curves in the top panel are for the isolated galaxy simulations with GALACTICS initial conditions while the green curves are for the simulations C.I.Ag run with AGAMA initial conditions. Bottom panel shows initial rotation curve decomposition for the runs D.I and E.II. .	57

4.2	The dimensionless ratio $\sigma_z^2/\pi G\Sigma z_d$ as a function of $\rho_h/\rho_0$ for the models considered in this paper (stars), the disc-halo models from Yurin and Springel (2015) (filled squares) and the model from Gauthier et al. (2006) (filled triangle). The straight line is the function $f = 1 + (2\pi/3)^{1/2} \rho_h/\rho_0$ discussed in the text. . . . .	59
4.3	Distribution of simulations considered in this paper in the $Q - X$ and the $z_d/R_d - \sigma_R/\sigma_z$ planes. Stars are simulations run for this paper (A-E); filled squares denote the series of simulations described in Yurin and Springel (2015); the filled triangle denotes the simulation of M31 run in Gauthier et al. (2006); open pentagons denote the simulations described in Widrow et al. (2008). . . . .	60
4.4	Strength and length of bars for the simulations considered in Gauthier et al. (2006). The twenty-five models span the $Q$ - $X$ plane. Top panel shows the $A_2$ parameter while the bottom panel shows the bar length. Both are measured at 5 Gyr (the final snapshot of the simulations). . .	61
4.5	Surface density maps for isolated galaxy simulations at select times. Time proceeds from 0 to 10 Gyr, left-to-right, and the models span top-to-bottom in order of their appearance in Table 4.1. The overlaid red circles have radii $R_p = 5.5$ kpc and 20 kpc. . . . .	62

4.6	Mean bar strength parameter inside a cylindrical radius $R_p$ , $A_2(< R_p)$ , as a function of time. Curves are smoothed in time with a top-hat moving window of width 1 Gyr. Line colors are blue, red, and green for models A, B, and C, respectively. Results for the fiducial runs A.I, B.I, and C.I are shown as solid curves while the results for the runs with high softening length, A.II and B.II, are shown as dashed curves. The AGAMA model C.I.Ag is shown as a dot-dashed curve. . . . .	63
4.7	Bar strength parameter $A_2$ as a function of radius and time. The trajectory of corotation is shown by the dashed red line. . . . .	64
4.8	Root mean square height $z_{\text{rms}}$ as a function of cylindrical radius $R$ for ten snapshots equally spaced over the first 500 Myr. Panels are for simulations A.I (upper left), A.II (upper right), C.I (lower left) and C.I.Ag (lower right). . . . .	65
4.9	Diagonal components of the velocity dispersion tensor and $z_{\text{rms}}$ as a function of $R$ for different snapshots between 0 and 10 Gyr. Shown, from top to bottom, are profiles for $z_{\text{rms}}$ , $\sigma_z$ , $\sigma_R$ , and $\sigma_\phi$ for the same size models included in Fig. 4.5. . . . .	66
4.10	Mean bar strength parameter inside the cylindrical radius $R_p$ , $A_2(< R_p)$ , as a function of time. The figure is essentially the same as Fig. 4.6 though this time we include simulations A.III, B.III, and C.III where buckling is suppressed. . . . .	80

4.11	Projections for the D.I (left three columns) and E.II (right three columns). The three columns for each simulation correspond,from left to right, to 2.2 Gyr, 5.9 Gyr, and 13.7 Gyr after the Big Bang. The overlaid red circles have radii $R_p$ and $20 h^{-1}$ kpc. . . . .	81
4.12	$A_2(< R_p)$ as a function of the age of the Universe for simulations D.I (solid curve) and E.II (dashed curve). . . . .	82
4.13	Fraction of particles with distance from the midplane greater than some distance $d$ as a function of $d$ . The difference colours correspond to different bins in cylindrical radius $R$ : $0 < R < 5$ kpc — black; $5 \text{ kpc} < R < 10 \text{ kpc}$ — blue; $10 \text{ kpc} < R < 15 \text{ kpc}$ — red; $15 \text{ kpc} <$ $R < 20 \text{ kpc}$ — green; $20 \text{ kpc} < R \text{ kpc}$ — magenta. . . . .	83

# Chapter 1

## Introduction

### 1.1 Section

#### 1.1.1 SubSection

##### SubSubSection

##### Paragraph

##### SubParagraph

### 1.2 Motivation

...the current de facto standard being the Unified Modeling Language (UML) ?...

### 1.3 Problem

### 1.4 Objective



Note: These are the section headings that I decided to use. Check out several recent theses to decide how you want to lay out your introduction (and conclusion) chapters.

### **1.4.1 Hypothesis**

## **1.5 Contributions**

## **1.6 Organization of Thesis**

We proceed by introducing conformance checking and discussing related work in the next chapter. We discuss the Alloy language and the Alloy Analyzer tool in Chapter ???. Chapter ?? describes our Embee tool, from the user's perspective, with several running examples. Implementation details and the analysis of the tool are presented in Chapter ??. Chapter 5 concludes and outlines future work.



## Chapter 2

### A Dynamical Recipe for Cosmological Disks

#### 2.1 Physical Motivation of Modeling

#### 2.2 Time Evolution of Collisionless Systems

##### 2.2.1 The Collisionless Boltzmann Equation

##### 2.2.2 Numerical Solutions

#### 2.3 Phase Space, Equilibrium, and Initial Conditions

##### 2.3.1 Jeans Modeling

##### 2.3.2 DF-based Models and the Strong Jeans Theorem

##### 2.3.3 Action-Angle Variables

##### 2.3.4 DFs as Functions of Actions

#### 2.4 Simulation Analysis: Paradigms and Tools

##### 2.4.1 WKB Wave Analysis

##### 2.4.2 Time Series Filtering

##### 2.4.3 MCMC

#### 2.5 Cosmology and Implications for Galaxy Studies

## Chapter 3

# A Method for Studying Discs in Cosmological Haloes

### 3.1 Abstract

We present a new method for embedding a stellar disc in a cosmological dark matter halo and provide a worked example from a  $\Lambda$ CDM zoom-in simulation. The disc is inserted into the halo at a redshift  $z = 3$  as a zero-mass rigid body. Its mass and size are then increased adiabatically while its position, velocity, and orientation are determined from rigid-body dynamics. At  $z = 1$ , the rigid disc is replaced by an N-body disc whose particles sample a three-integral distribution function (DF). The simulation then proceeds to  $z = 0$  with live disc and halo particles. By comparison, other methods assume one or more of the following: the centre of the rigid disc during the growth phase is pinned to the minimum of the halo potential, the orientation of the rigid disc is fixed, or the live N-body disc is constructed from a two rather than three-integral DF. In general, the presence of a disc makes the halo rounder, more centrally concentrated, and smoother, especially in the innermost regions. We find that methods in which the disc is pinned to the minimum of the halo potential tend

to overestimate the amount of adiabatic contraction. Additionally, the effect of the disc on the subhalo distribution appears to be rather insensitive to the disc insertion method. The live disc in our simulation develops a bar that is consistent with the bars seen in late-type spiral galaxies. In addition, particles from the disc are launched or “kicked up” to high galactic latitudes.

### 3.2 Introduction

The structure and evolution of galaxies are determined by the spectrum of primordial density perturbations, the dynamics of stars and dark matter, and baryonic physics. Over the past two decades, there has been a concerted effort to incorporate the latter into cosmological simulations (e.g. Katz et al., 1996; Springel and Hernquist, 2003; Stinson et al., 2006; Roškar et al., 2010; Pakmor and Springel, 2013; Gómez et al., 2016). While these simulations have enhanced our understanding of galaxy formation, their computational cost is high. Adding to the challenge is the complex and sub-grid nature of star formation, supernova feedback, and other baryonic processes, which require *ad hoc* parametric models.

In this work, we focus on the dynamics of disc galaxies. Our goal is to study the nature of disc-halo interactions where it is advantageous to be able to control properties of the disc such as its mass, size, and internal kinematics. Such control is not possible in *ab initio* simulations.

Simulations of isolated disc galaxies provide an alternative arena to study galactic structure and dynamics. Moreover, many aspects of disc-halo interactions can be understood by considering the collisionless dynamics of stars and dark matter while

ignoring gas physics. For example, simulations of stellar disc-bulge systems embedded in dark haloes have proved indispensable in studies of bar and spiral structure formation (See Sellwood (2013) and references therein). These simulations typically begin with systems that are in equilibrium, or nearly so. For this reason, they usually assume axisymmetric initial conditions, which are manifestly artificial. In short, discs do not come into existence as formed, highly symmetric objects but rather build up through the combined effects of gas accretion, star formation, and feedback (Vogelsberger et al., 2013; Schaye et al., 2015). Moreover, the haloes in which the real discs reside are almost certainly triaxial and clumpy (Navarro et al., 1997; Moore et al., 1999; Klypin et al., 1999).

There now exists a long history of attempts to bridge the gap between simulations of isolated disc-bulge-halo systems, with their pristine initial conditions, and cosmological simulations. Kazantzidis et al. (2008), for example, followed the evolution of a Milky Way-like disc in its encounter with a series of satellites whose properties were motivated by cosmological simulations. They found that the satellites “heated” the disc and prompted the formation of a bar and spiral structure. Along similar lines, Purcell et al. (2011) modeled the response of the Milky Way to the gravitational effects of the Sagittarius dwarf galaxy (Sgr) by simulating disc-satellite encounters for different choices of the satellite mass. They concluded that Sgr may have triggered the development of the spiral structure seen in the Milky Way today. Continuing in this vein, Laporte et al. (2016) studied the influence of the Large Magellanic Cloud and Sgr on the Milky Way disc and found that they can create similar warps to what has been observed. The effect of a time-dependent triaxial halo was investigated in Hu and Sijacki (2016) where they found it can trigger grand-design spiral arms.

Of course, the disc of the Milky Way lives within a population of satellite galaxies and, quite possibly, pure dark matter subhaloes (Moore et al., 1999; Klypin et al., 1999). With this in mind Font et al. (2001) simulated the evolution of an isolated disc-bulge-halo model where the halo was populated by several hundred subhaloes. They concluded that that substructure played only a minor role in heating the disc, a result that would seem at odds with those of Kazantzidis et al. (2008). Numerical simulations by Gauthier et al. (2006) and Dubinski et al. (2008) shed some light on this discrepancy. In those simulations, 10% of the halo mass in an isolated disc-bulge-halo system was replaced by subhaloes with a mass distribution motivated by the cosmological studies of Gao et al. (2004). Gauthier et al. (2006) found that a modest amount of disc heating occurred during the first 5 Gyr, at which point satellite interactions prompted the formation of a bar, which in turn heated the disc more significantly. Not surprisingly, the timing of bar formation varied from 1 Gyr to 10 Gyr when the experiment was repeated with different initial conditions for the satellites.

The aforementioned simulations have several drawbacks. First, most of them do not allow for halo triaxiality. Second, the disc is initialized at its present-day mass whereas real discs form over several Gyr. Finally, the subhaloes are inserted into the halo in an *ad hoc* fashion. Several attempts have been made to grow a stellar disc in a cosmological halo in an effort to address these shortcomings (Berentzen and Shlosman, 2006; DeBuhr et al., 2012; Yurin and Springel, 2015). The general scheme proceeds in three stages. During the first stage, a cosmological simulation is run with pure dark matter and a suitable halo is selected. In the second, a rigid disc potential is grown slowly in the desired halo, thus allowing the halo particles

to respond adiabatically to the disc’s time-varying potential. In the third stage, the rigid disc is replaced by a live one and the simulation proceeds with live disc and halo particles.

DeBuhr et al. (2012) used such a scheme to introduce stellar discs into dark matter haloes from the Aquarius Project (Springel et al., 2008). They added a rigid disc at a redshift  $z = 1.3$  with a mass parameter for the disc that grew linearly with the scale factor from an initial value of zero to its final value at  $z = 1$ . The disc was initially centered on the potential minimum of the halo and oriented so that its symmetry axis pointed along either the minor or major axis of the halo. During the rigid disc phase, the motion of the disc centre of mass was determined from Newton’s 3rd law. To initialize the live disc, DeBuhr et al. (2012) approximate the halo potential as a flattened, axisymmetric logarithmic potential and then determine the disc distribution function (DF) by solving the Jeans equations.

Yurin and Springel (2015) introduced a number of improvements to this scheme. Most notably, they use GALIC to initialize the live disc (Yurin and Springel, 2014). This code is based on an iterative scheme for finding stationary solutions to the collisionless Boltzmann equation. The general idea for iterative codes is to begin with a set of particles that has the desired spatial distribution and some initial guess for the velocity distribution. The velocities are then adjusted so as to achieve stationarity, as measured by evolving the system and computing a certain merit function. In Yurin and Springel (2015) the initial disc was assumed to be axisymmetric with a DF that depended on two integrals of motion, the energy,  $E$ , and angular momentum,  $L_z$ . One striking, if not puzzling, result from this work is the propensity of the discs to form very strong bars. These bars are especially common in models without bulges



even in cases where the disc is submaximal.

In this paper, we introduce an improved scheme for inserting a live disc in a cosmological halo. In particular, the centre of mass *and* orientation of the rigid disc are determined by solving the standard equations of rigid body dynamics. Thus, our rigid disc can undergo precession and nutation. The angular and linear velocities of the rigid disc at the end of the growth phase are incorporated into the live disc initial conditions. As in Yurin and Springel (2015) we use an axisymmetric approximation for the halo potential when constructing the disc DF. However, our DF is constructed from an analytic function of  $E$ ,  $L_z$ , and the vertical energy  $E_z$ , which is an approximate integral of motion used in GALACTICS (Dubinski and Kuijken, 1995; Widrow et al., 2008). By design, the disc DF yields a model whose density has the exponential-sech<sup>2</sup> form. And with a three-integral DF, we have sufficient flexibility to model realistic Milky Way-like discs. As discussed below, the initial disc DF may be crucial in understanding the formation of the bar.

As a demonstration of our method we grow a Milky Way-like disc in an approximately  $10^{12} h^{-1} M_\odot$  halo from a cosmological zoom-in simulation. We discuss both disc dynamics and the effect our disc has on the population of subhaloes. Discs have been invoked as a means of depleting halo substructure and thus alleviating the Missing Satellite Problem, which refers to the underabundance of observed Milky Way satellites relative to the number of Cold Dark Matter subhaloes seen in simulations (Moore et al., 1999; Klypin et al., 1999). An earlier study by D’Onghia et al. (2010) found that when a disc potential is grown in a Milky Way-size cosmological halo, the abundance of substructure in the mass range  $10^7 M_\odot$  to  $10^9 M_\odot$  was reduced by a factor of 2 – 3. Similar results were found by Sawala et al. (2017) and Garrison-Kimmel

	DMO	MN	FO	RD	LD
$M_d (M_\odot)$	–	$7.2 \times 10^{10}$	$7.2 \times 10^{10}$	$7.2 \times 10^{10}$	$7.2 \times 10^{10}$
$R_{d,0}$ (kpc)	–	3.7	3.7	3.7	3.7
$N_d$	–	–	$10^6$	$10^6$	$10^6$
$z_g$	–	3.0	3.0	3.0	–
$z_l$	–	1.0	1.0	1.0	1.0
$N_r$	4096	4096	4096	4096	4096
$L_{box}$ ( Mpc $h^{-1}$ )	50	50	50	50	50

Table 3.1: A summary of the simulation parameters, as discussed in the text.  $M_d$  is the final disk mass,  $R_{d,0}$  is the final disk scale radius,  $N_d$  is the number of particles used to simulate the disk,  $z_g$  and  $z_l$  are the redshifts when the disk begins to grow and when it becomes live (respectively),  $N_r$  is the effective resolution in the zoom-in region, and  $L_{box}$  is the comoving size of the box.

et al. (2017).

The organization of the paper is as follows. In Section 2, we outline our method for inserting a live disc into a cosmological simulation. We also present results from a test-bed simulation where a disc is inserted into an isolated flattened halo. We next apply our method to a cosmological zoom-in simulation. In Section 3, we focus on disc dynamics and find that the disc develops a bar, spiral structure and a warp. In addition, disc-halo interactions appear to “kick” stars out of the disc and into regions normally associated with the stellar halo. In Section 4, we present our results for the spherically-averaged density profile and shape of the dark matter halo as well as the distribution of subhaloes. Particular attention is paid to the sensitivity of these results to the disc insertion scheme. We conclude in Section 5 with a summary and discuss possible applications of this work.

### 3.3 Inserting a Stellar Disc into a Cosmological Halo

In this section, we detail our method for inserting a live stellar disc into a cosmological simulation. We begin with an overview of our approach and the five main simulations presented in this paper. We then describe some of the more technical aspects of the method.

#### 3.3.1 Overview of Simulation Set

Our simulations are performed with the N-body component of GADGET-3, which is an updated version of GADGET-2 (Springel, 2005). For the cosmological simulations, we implement the zoom-in technique of Katz et al. (1994) and Navarro et al. (1994), broadly following the recommendations of Oñorbe et al. (2014), which allows us to achieve very high spatial and mass resolution for a single halo while still accounting for the effects of large-scale tidal fields. For the cosmological parameters, we use the results from Planck 2013 (Planck Collaboration et al., 2014) with  $h = 0.679$ ,  $\Omega_b = 0.0481$ ,  $\Omega_0 = 0.306$ ,  $\Omega_\Lambda = 0.694$ ,  $\sigma_8 = 0.827$ , and  $n_s = 0.962$ .

We begin by simulating a  $50 h^{-1}\text{Mpc}$  box with  $N_r = 512^3$  particles, where  $N_r$  is the effective resolution, each with a mass of  $\sim 7.9 \times 10^7 h^{-1} M_\odot$ . We identify a Milky Way-like halo in the present-day snapshot, that is, a  $\sim 10^{12} M_\odot$  halo which has experienced no major mergers since  $z = 1$  and which has no haloes with  $2h^{-1}\text{Mpc}$  more than half the mass of the MW-analogue. We then run an intermediate zoom-in simulation targeting all particles within 10 virial radii of the low resolution halo. The initial conditions for this simulation are generated with MUSIC (Hahn and Abel, 2013), which creates five nested regions from a coarse resolution of  $N_r = 128^3$  in the outskirts to an effective  $N_r = 2048^3$  resolution in the targeted region. After this

simulation reaches  $z = 0$ , we select all particles within 7.5 virial radii and regenerate initial conditions with one more level of refinement, giving six nested zoom regions, where now, the highest effective resolution is  $N_r = 4096^3$ . Our final halo is composed of approximately  $10^7$  particles, each with a mass of  $1.54 \times 10^5 h^{-1} M_\odot$ . The softening lengths were selected using the criteria in Power et al. (2003) with a softening of 719 comoving pc for the highest resolution particles in the final zoom-in simulation. We found that this repeated zoom-in technique results in remarkably little contamination from coarse resolution particles within the targeted halo, giving a clean region of size  $1.9h^{-1}$  Mpc at  $z = 0$ .

The dark matter only (DMO) simulation not only serves as the basis for four simulations with discs but also provides a control “experiment” for our study of the effect discs have on halo properties. In each of our disc simulations, the potential of a rigid disc is introduced at the “growing disc” redshift  $z_g$ . The mass parameter of the disc is then increased linearly with the scale factor  $a = 1/(1+z)$  from zero to its final value  $M_d$  at the “live disc” redshift  $z_l$ . As described in Sec. 3.3.5, the radial and vertical scale lengths of the disc are also increased between  $z_g$  and  $z_l$  to account for the fact that discs grow in scale as well as mass while they are being assembled.

In the first of our disc-halo simulations, dubbed MN, we introduce a rigid Miyamoto-Nagai disc (Miyamoto and Nagai, 1975), whose gravitational potential is given by

$$\Phi(R, z) = -\frac{GM_d}{\left(R^2 + \left(R_d + (z^2 + z_d^2)^{1/2}\right)^2\right)^{1/2}}. \quad (3.1)$$

For this simulation, which was meant to mimic the scheme in D’Onghia et al. (2010), we assume that the centre of the disc tracks the minimum of the halo potential while

the orientation of the disc is fixed to be aligned with the  $z$ -axis of the simulation box. Note that this is effectively a random direction for the halo.

In the remaining three disc simulations, we grow an exponential-sech<sup>2</sup> rigid disc potential in our halo with mass and scale-length parameters that grow in time. For our fixed-orientation (FO) simulation, the position and velocity of the disc’s centre of mass are determined from Newtonian dynamics while the spin axis of the disc is initially aligned with the minor axis of the halo at  $z = z_g$  and kept fixed in the simulation box frame thereafter. In this respect, the simulation is similar to the ones presented in DeBuhr et al. (2012) and Yurin and Springel (2015). For the rigid-disc (RD) simulation the disc’s orientation, which is now a function of time, is determined from Euler’s rigid body equations.

In the MN, FO, and RD runs, we continue the simulation to the present epoch ( $z = 0$ ) with the assumed rigid disc potential where the mass and scale length parameters are held fixed and the position and orientation are calculated as they were during the growth phase. For our final live disc (LD) simulation, we swap a live disc for the RD disc at  $z_l$ . Thus, the RD and LD simulations are identical prior to  $z_l$ . All of our discs have a final mass of  $M_d = 7.2 \times 10^{10} M_\odot$ , a final scale radius of 3.7 kpc, and a final scale height of 0.44 kpc. Our simulation parameters can be found summarized in Table 3.1.

#### 3.3.2 Summary of Live Disc Insertion Scheme

The first step in our disc insertion scheme is to calculate an axisymmetric approximation to the gravitational potential of the DMO halo at  $z = 0$ . We do so using an expansion in Legendre polynomials as described below. We then generate a particle

representation of a stellar disc that is in equilibrium with this potential using the GALACTICS code (Kuijken and Gilmore, 1989; Widrow et al., 2008). Though GALACTICS allows one to generate the phase space coordinates of the disc stars, at this stage, we only need the positions of the stars, which we use to represent the “rigid disc”. At the  $z_g$  snapshot, we incorporate the disc particles into the mass distribution of the system with the disc centered on the potential minimum of the halo. We then rerun the simulation from  $z_g$  to  $z_l$  with the following provisos. First, the mass of the disc is increased linearly with  $a$  from zero to its final value. Second, the size of the disc increases with time, which we account for by having the positions of the disc particles, as measured in the disc frame, expand with time to their final values at  $z_l$ . Finally, the center of mass and orientation of the disc are determined by integrating the equations of rigid-body dynamics. At redshift  $z_l$ , the DF of the disc is recalculated assuming the same structural parameters as before but with an axisymmetric approximation to the new halo potential. An N-body disc is generated from this DF and the simulation proceeds with live disc particles. In this paper, we choose  $z_g = 3$  and  $z_l = 1$  so that the growth period lasts from 2.2 Gyr to 5.9 Gyr after the Big Bang. This period in time roughly corresponds to the epoch of peak star formation in Milky Way-like galaxies (e.g. van Dokkum et al., 2013).

Our simulations during this epoch can be used to study the effect of a disc potential on the evolution of substructure. On the other hand, our simulations of the live disc epoch ( $z_l > z > 0$ ) can also be used to study disc dynamics in a cosmologically-motivated dark halo.

### 3.3.3 Halo Potential

Our method requires an axisymmetric approximation to the halo potential centred on the disc. This approximation is found using an expansion in spherical harmonics (see Binney and Tremaine (2008)) where only the  $m = 0$  terms are included. The potential is then expressed as an expansion in Legendre polynomials. We divide the region that surrounds the disc into spherical shells and calculate the quantities

$$m_{l,i} = \sum_{n \in S_i} m_n P_l(\cos \theta_n), \quad (3.2)$$

where the sum is over the halo particles of mass  $m_n$  in the  $i$ 'th shell ( $S_i$ ),  $P_l$  are the Legendre polynomials, and  $(r, \theta, \phi)$  are spherical polar coordinates centred on the disc. The axisymmetric approximation to the potential is then

$$\Phi_h(r, \theta) = \sum_{l=0}^{\infty} A_l(r) P_l(\cos \theta) \quad (3.3)$$

where

$$A_l(r) = -G \left( \frac{1}{r^l} \int_0^r dr' r'^{l+2} m_l(r') + r^{l+1} \int_0^r dr' r'^{1-l} m_l(r') \right) \quad (3.4)$$

and  $m_l$  is given by Eq. (3.2) for sufficiently small radial bins.

### 3.3.4 Disc DFs

Armed with an axisymmetric approximation to the halo potential, we construct a self-consistent DF for the disc following the method outlined in Dubinski and Kuijken (1995). This DF is an analytic function of  $E$ ,  $L_z$ , and  $E_z$ . By construction, the DF

yields a density law for the disc which is, to a good approximation, given by

$$\rho_d(R, z) \simeq \frac{M_d}{4\pi R_d^2 z_d} e^{-R/R_d} \text{sech}^2(z/z_d) T(R_t, \Delta_t) \quad (3.5)$$

where  $M_d$ ,  $R_d$ , and  $z_d$  are the mass, radial scale length and vertical scale height of the disc and  $R = \sqrt{r^2 - z^2}$ . The truncation function  $T$  insures that the density falls rapidly to zero at a radius  $R_t + \Delta_t$ . The square of the radial velocity dispersion is chosen to be proportional to the surface density, that is,  $\sigma_R = \sigma_{R0} \exp(-R/2R_d)$ . The central velocity dispersion  $\sigma_{R0}$  controls, among other things, the Toomre  $Q$  parameter and thus the susceptibility of the disc to instabilities in the disc plane. The azimuthal velocity dispersion is calculated from the radial velocity dispersion through the epicycle approximation (for details see Binney and Tremaine, 2008) while the vertical velocity dispersion is adjusted to yield a constant scale height  $z_d$ . We stress that although the density law is written as a function of  $R$  and  $z$ , which are not integrals of motion, the underlying DF is a function of  $E$ ,  $L_z$ , and  $E_z$ , which are integrals of motion to the extent that the epicycle approximation is valid and that the potential can be approximated by an axisymmetric function.

### 3.3.5 Rigid Disc Dynamics

During the disc growth phase, the disc mass is given by

$$M(a) = M_d \left( \frac{a - a_g}{a_l - a_g} \right), \quad (3.6)$$

where  $a_g$  is the scale factor evaluated at  $z_g$ . The positions of the disc particles expand self-similarly in disc or body coordinates. That is, the comoving position of a disc particle in body coordinates is given by  $\mathbf{s}_i(a) = b(a)\mathbf{s}_i(a_l)$  where  $\mathbf{s}_i(a)$  is the comoving



position of the  $i$ 'th disc particle in the body frame

$$b(a) = b_g + (1 - b_g) \left( \frac{a - a_g}{a_l - a_g} \right), \quad (3.7)$$

where  $b_g = b(a_g)$ , and we choose  $b_g = 0.1$ . The angular velocity of the disc is described by the vector  $\boldsymbol{\omega} = (\omega_x, \omega_y, \omega_z)$  where  $\omega_z$  corresponds to the spin of the disc about its symmetry axis. We assume that

$$\omega_z(a) = \omega_z(a_l) \left( \frac{M(a)}{M_d} \right)^{1/\alpha} b(a), \quad (3.8)$$

which insures that the disc tracks the Tully-Fisher relation,  $M_d \propto V_d^\alpha \propto (\omega_3 R_d)^\alpha$  (Torres-Flores et al., 2011). In this work we set  $\alpha = 3.5$ .

The orientation of the disc is described by its Euler angles. We follow the convention of Thornton and Marion (2008) and use  $\phi$ ,  $\theta$ , and  $\psi$  where the matrix

$$\mathcal{R} = \mathcal{R}_z(\phi) \mathcal{R}_y(\theta) \mathcal{R}_z(\psi) \quad (3.9)$$

describes the transformation from the disc body frame to the simulation frame. Here  $\mathcal{R}_i(\alpha)$  is the matrix for a rotation by angle  $\alpha$  about the  $i$ 'th axis. Physically, changes in  $\phi$  and  $\theta$  correspond to precession and nutation, respectively while  $\psi$  is a degenerate rotation about the disc's symmetry axis. The equations of motion for the Euler angles and angular velocity of the disc, which must account for the time-dependence of the disc's moment of inertia as well as the fact that GADGET-3 uses comoving coordinates, are derived in Appendix A. These equations allow us to solve for the orientation of the disc under the influence of torque due to dark matter.

At the end of the growth phase, we initialize the disc with a DF that is recalculated

using GALACTICS. As we will see, during the growth phase the motion of the disc involves a mix of precession and nutation. In general, a live disc is not able to support the sort of rapid nutation seen in the rigid disc, essentially because different parts of the disc respond to torques from the halo and the disc itself differently. We therefore initialize the live disc with an orientation and precessional motion given by a fixed-window moving average of the rigid disc coordinates.

### 3.3.6 Test-bed Simulation of an Isolated Galaxy

We test our method by growing a stellar disc in an isolated, flattened halo in a non-cosmological simulation. To initialize the flattened halo we first generate a particle realization of a truncated, spherically symmetric NFW halo (Navarro et al., 1997) whose density profile is given by

$$\rho(r) = \frac{v_h^2 a_h}{4\pi G r} \frac{1}{(r + a_h)^2} \quad (3.10)$$

with  $a_h = 8 \text{ kpc}$  and  $v_h = 400 \text{ km s}^{-1}$ . The halo is truncated at a radius much larger than the radius of the disc. The  $z$  and  $v_z$  coordinates are then reduced by a factor of two and the system is evolved until it reaches approximate equilibrium. The result is an oblate halo with an axis ratio of  $\sim 0.8$  and a symmetry axis that coincides with the  $z$ -axis of the simulation box. We next grow a rigid disc over a period of 1 Gyr to a final mass of  $4.9 \times 10^{10} M_\odot$  and final radial and vertical scale lengths of  $R_d = 2.5 \text{ kpc}$  and  $z_d = 200 \text{ pc}$ , respectively. The disc is grown at an incline of  $30^\circ$  relative to the symmetry plane of the halo. Doing so allows us to check the rigid body integration scheme for a case when the symmetry axes of the disc and halo are initially misaligned. At  $t = 1 \text{ Gyr}$  we replace the rigid disc with a live one and

evolve the system for an additional 1 Gyr. In a separate simulation, we also follow the evolution of the rigid disc over the same time period, allowing us to compare the evolution of the live and rigid disc.

Fig. 3.1 shows the Euler angles and angular velocity components for the rigid and live discs as a function of time. The time-dependence of  $\omega_x$  and  $\omega_y$  is characterized by an interference pattern between short  $\sim 125$  Myr period nutations and a decaying long-period precessional motion. Note that  $\theta$  and  $\phi$  for the live disc track the corresponding values for the rigid disc for  $t > 1$  Gyr. By initializing the live disc with the angular velocity of the rigid disc, we capture the (small) precessional motion of  $\sim 10^\circ \text{Gyr}^{-1}$  between  $t = 1$  Gyr and 2 Gyr. The disc settles into a preferred plane within the first 300 Myr that is intermediate between its initial symmetry plane and the initial symmetry plane of the halo. More precisely, the vector of the new minor axis is  $\mathbf{c} = [-0.159, 0.146, 0.976]$  measured at 20 kpc,  $12.5^\circ$  from the original flattening axis.

Fig. 3.2 shows surface density maps for the disc at two snapshots. The disc develops a weak warp due to its interaction with the halo. The development of the warp is also evident in the surface density, vertical velocity dispersion, and scale height profiles shown in Fig. 3.3. We see that the surface density within  $\sim 15$  kpc or  $6R_d$  is essentially unchanged while at larger radii, there are 10 – 20% time-dependent fluctuations. The scale height  $\langle z^2 \rangle^{1/2}$  increases with time and radius. At early times, the increase is most prominent beyond  $\sim 15$  kpc while at late times, the scale height increases more smoothly from the center to the edge of the disc.

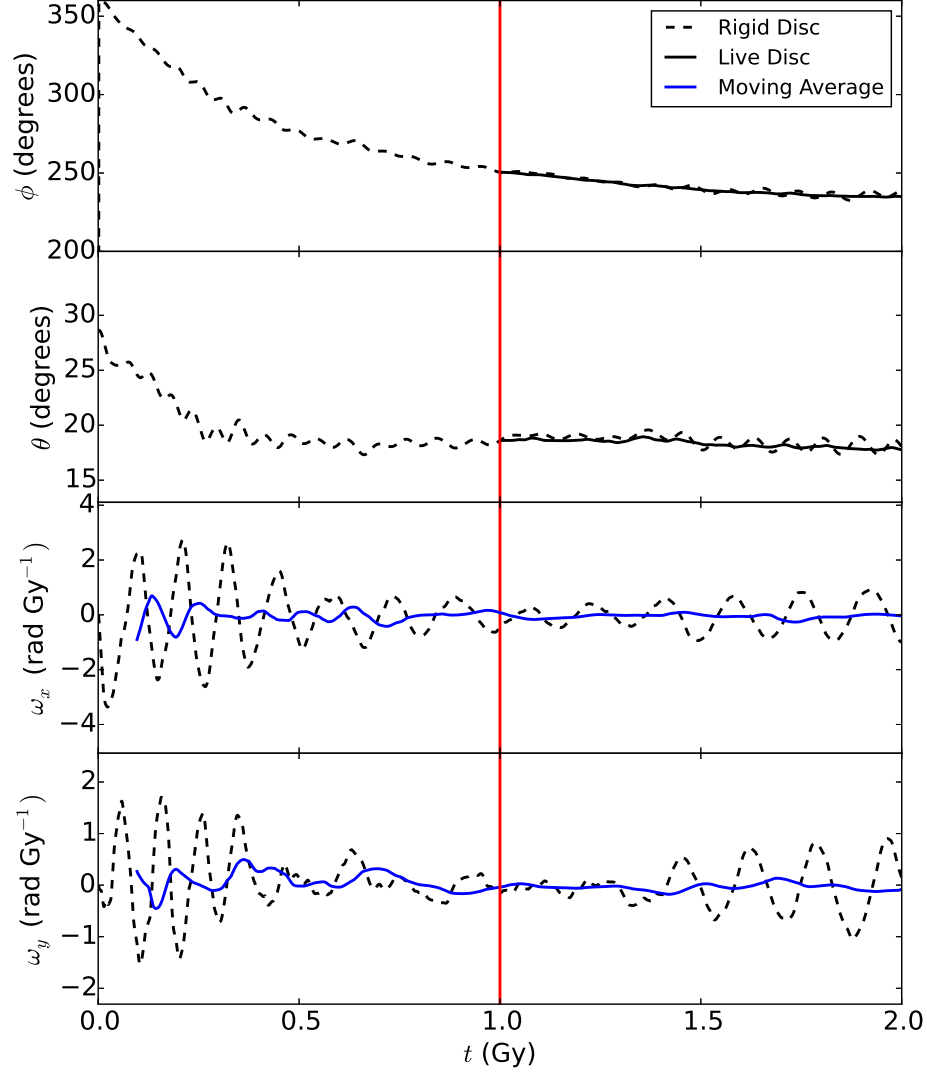


Figure 3.1: Kinematic variables for the rigid and live discs in an isolated, flattened halo as a function of time. The upper two panels show the Euler angles  $\theta$  and  $\phi$  for the rigid disc (dashed curves) and live disc (solid curves) where the live disc is introduced at  $t = 1$  Gyr (red vertical line). The bottom two panels show the  $x$  and  $y$  components of the angular velocity, as measured in the body coordinate system. In these two panels the solid curves show the  $\delta t \sim 150$  My moving average, which is used to initialize the live disc.

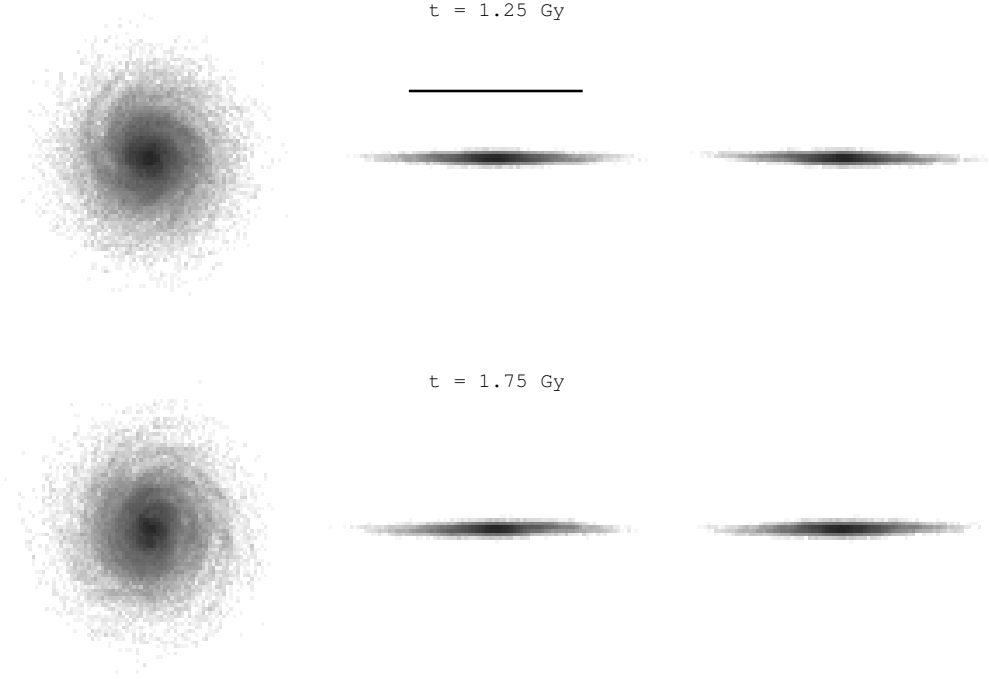


Figure 3.2: Face-on projections of the particle distribution for two snapshots of a live disc in a flattened halo. The solid line for scale is 25 kpc with a centre coincident with the disc's.

### 3.4 Cosmological Simulations

We now use our method to insert a live disc with prescribed structural properties into a cosmological halo. In this section, we focus on disc dynamics while in the next, we consider the effect the disc has on the dark halo.

In Fig. 3.4 we show the kinematic variables for the rigid and live discs in the RD and LD simulations. The two simulations are identical prior to  $z = 1$  ( $a = 0.5$ ) when the live disc is swapped in for the rigid one. The short period (300 Myr) oscillations in  $\omega_1$  and  $\omega_2$  are nutations. To initialize the live disc, we use the fixed-window moving average of  $\omega_x$  and  $\omega_y$ . By and large, the Euler angles of the rigid and live disc's track

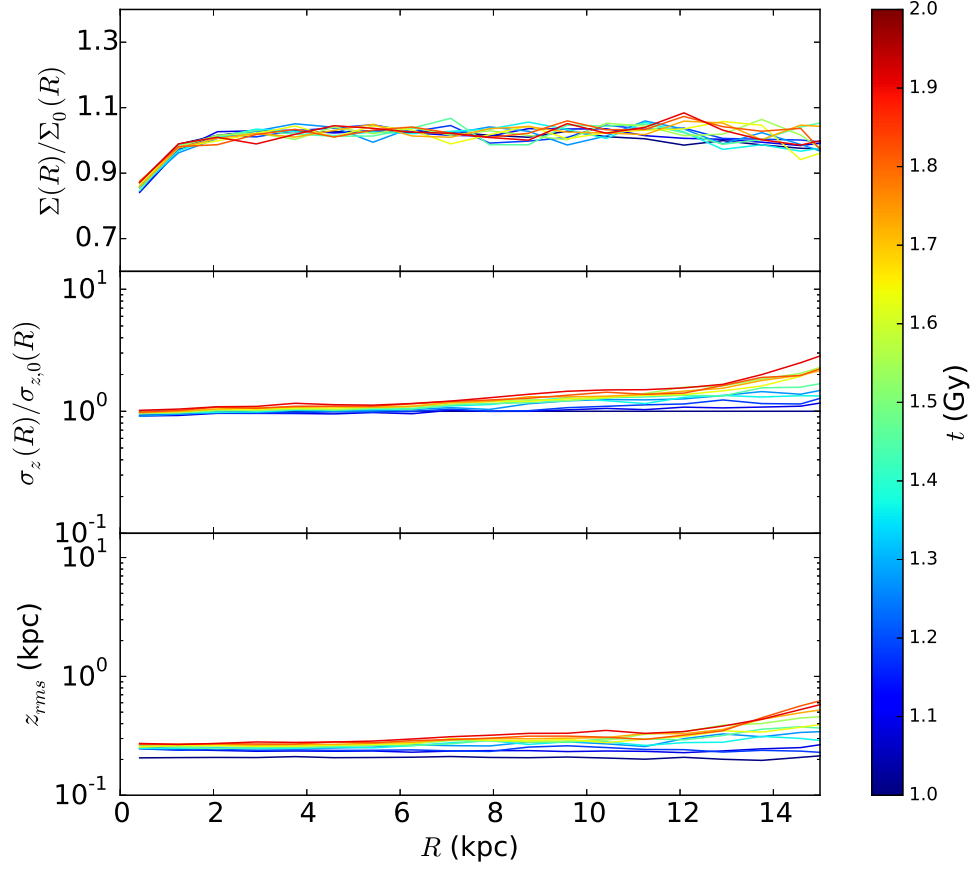


Figure 3.3: Surface density, vertical velocity dispersion, and scale height profiles as a function of Galactocentric radius  $R$  for 10 snapshots equally spaced in time. The top panel shows the surface density  $\Sigma(R)$  divided by  $\Sigma_0(R) = (M_d/2\pi R_d^2) \exp[-(R/R_d)]$  in order to highlight departures from a pure exponential disc. Likewise, in the middle panel, we show the ratio  $\sigma_z(R)/\sigma_{z,0}(R)$  where  $\sigma_{z,0} = \exp(-R/2R_d)$ . The bottom panel shows the RMS  $z$  as a function of  $R$ .

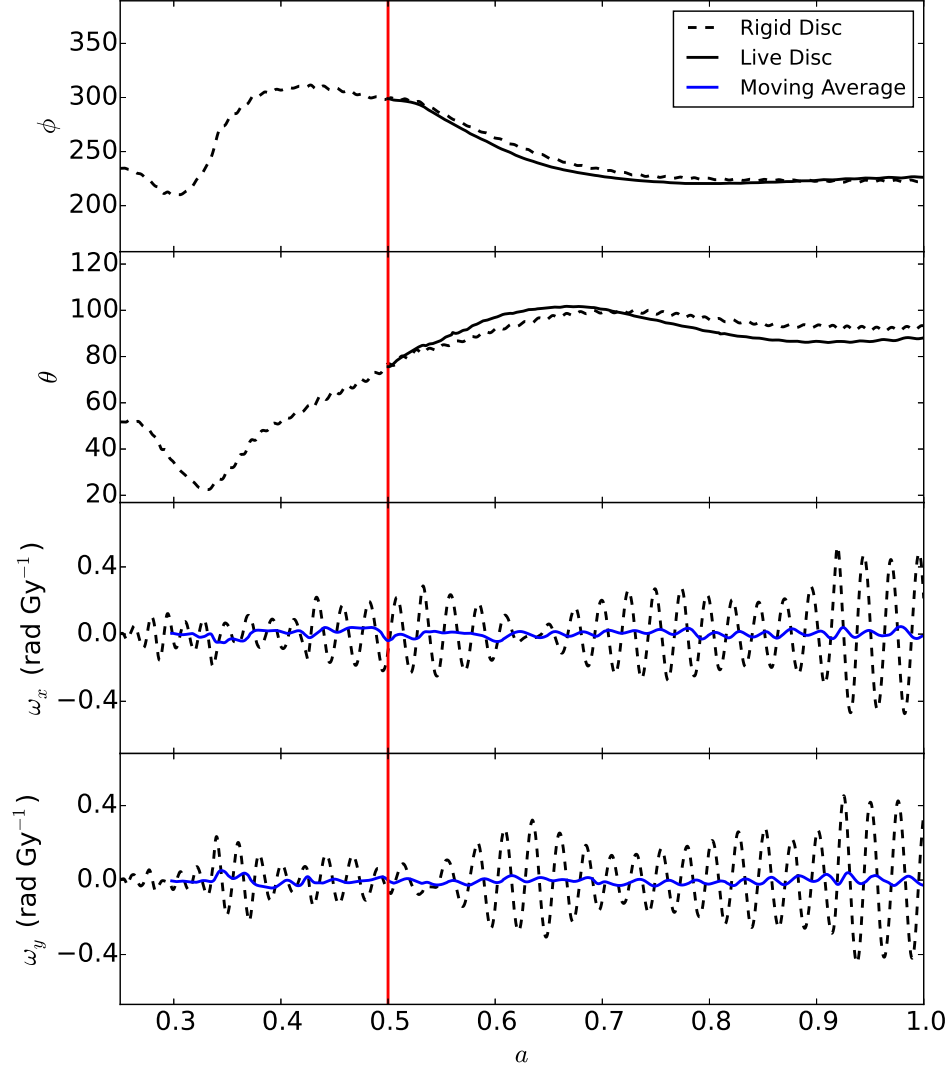


Figure 3.4: Kinematic variables for the rigid and live discs in our cosmological halo as a function of scale factor  $a$ . Line types are the same as in Fig. 3.1. The live disc is introduced at a redshift  $z = 1$  when the scale factor is  $a = 0.5$  (red vertical line). The blue line shows the  $\delta a \sim 0.04$  moving average calculated by averaging the last 300 points in the disc integration routine.

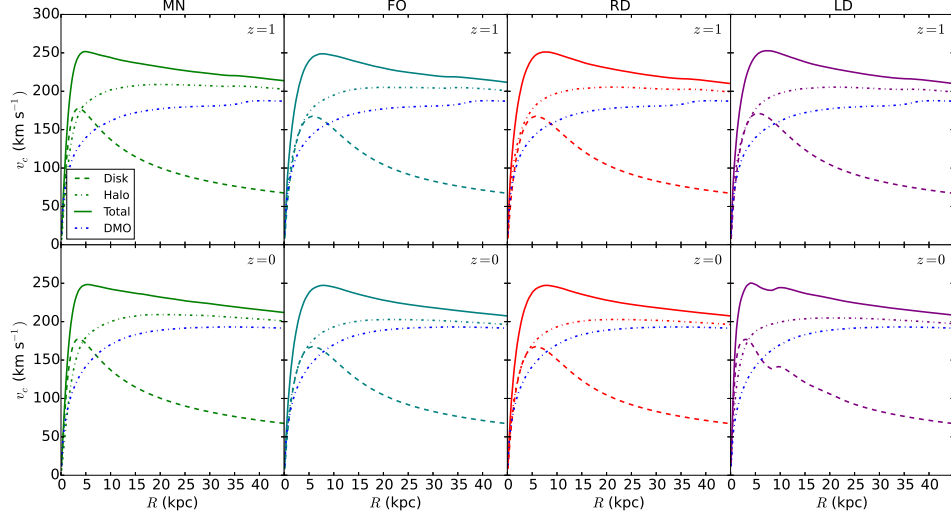


Figure 3.5: Circular speed curve decompositions at  $z = 1$  (top row) and  $z = 0$  (bottom row) for (from left to right) our LD, RD, and MN simulations. Halo contributions are represented as dot-dashed lines, disc contributions are represented by dashed lines, and the total rotation curve is given by a solid line. For reference, we have included the circular speed curve for the DMO halo (dot-dashed curve).

one another for  $z < 1$ , indicating that the rigid disc is a reasonable model for a live one, at least in terms of the disc’s orientation.

In Fig. 3.5 we show the circular speed curves at  $z = 1$  and  $z = 0$  for our four simulations. We see that the disc in our model is submaximal. To be precise, we have  $V_d/V_c \simeq 0.68$  at  $R = 2.2R_d$  where  $V_d$  is the circular speed due to the disc and  $V_c$  is the total circular speed. In short, the contributions from the disc and halo to the centrifugal force are approximately equal at a radius where the disc contribution reaches its peak value. By comparison, a maximal disc is generally defined to have  $V_d/V_c > 0.85$  (Sackett, 1997). If we use  $V_d/V_c$  at  $2.2R_d$  as the defining characteristic of the model, then our simulations match up with the F-5 simulation of Yurin and



Springel (2015), although our discs are slightly warmer, with a Toomre  $Q$ -parameter of 1.4 as compared with  $Q \simeq 0.9$  for their discs and our discs are thinner (200 pc vs. 600 pc). We note that in a two-integral disc DF,  $Q$  and the disc thickness are linked whereas in a three-integral DF, they can be set independently. The method of Yurin and Springel (2014) can be extended to consider a three-integral DF, but these models were not considered in Yurin and Springel (2015). Moreover, their two-integral model, which imposes  $\sigma_R = \sigma_z$ , violates the epicycle approximation, leading to transient system behaviour at early times when disc bars first form.

The circular speed curves in Fig. 3.5 show little change exterior to  $\sim 2R_d$  after  $z_l$ , thus providing another indication that the live disc was close equilibrium when it was swapped in for the rigid one. The formation of a bar is evident in the circular speed, and we can infer the bar contributes substantially inside  $2.2R_d \simeq 8$  kpc. The halo contribution at  $R = 2.2R_d$  is about 20% larger in the four disc runs than in the DMO one due to adiabatic contraction. Interestingly, the halo in the MN run shows somewhat more contraction than in the RD and LD runs. We note that in the MN run, the disc potential tracks the potential minimum of the halo whereas in the RD/LD case, the disc's position is determined from Newtonian dynamics. In general, the centre of the disc tracks the halo potential minimum so long as the potential changes slowly with time. However, during a major merger (and indeed, just such an event occurs at  $z = 2$ ) there are rapid changes in the halo potential and the position of the disc, as determined by Newtonian dynamics, can differ significantly from the minimum of the halo potential. Evidently, the *ad hoc* prescription of growing a disc at the halo's potential minimum may, in some cases, over-estimate the effect of adiabatic contraction.

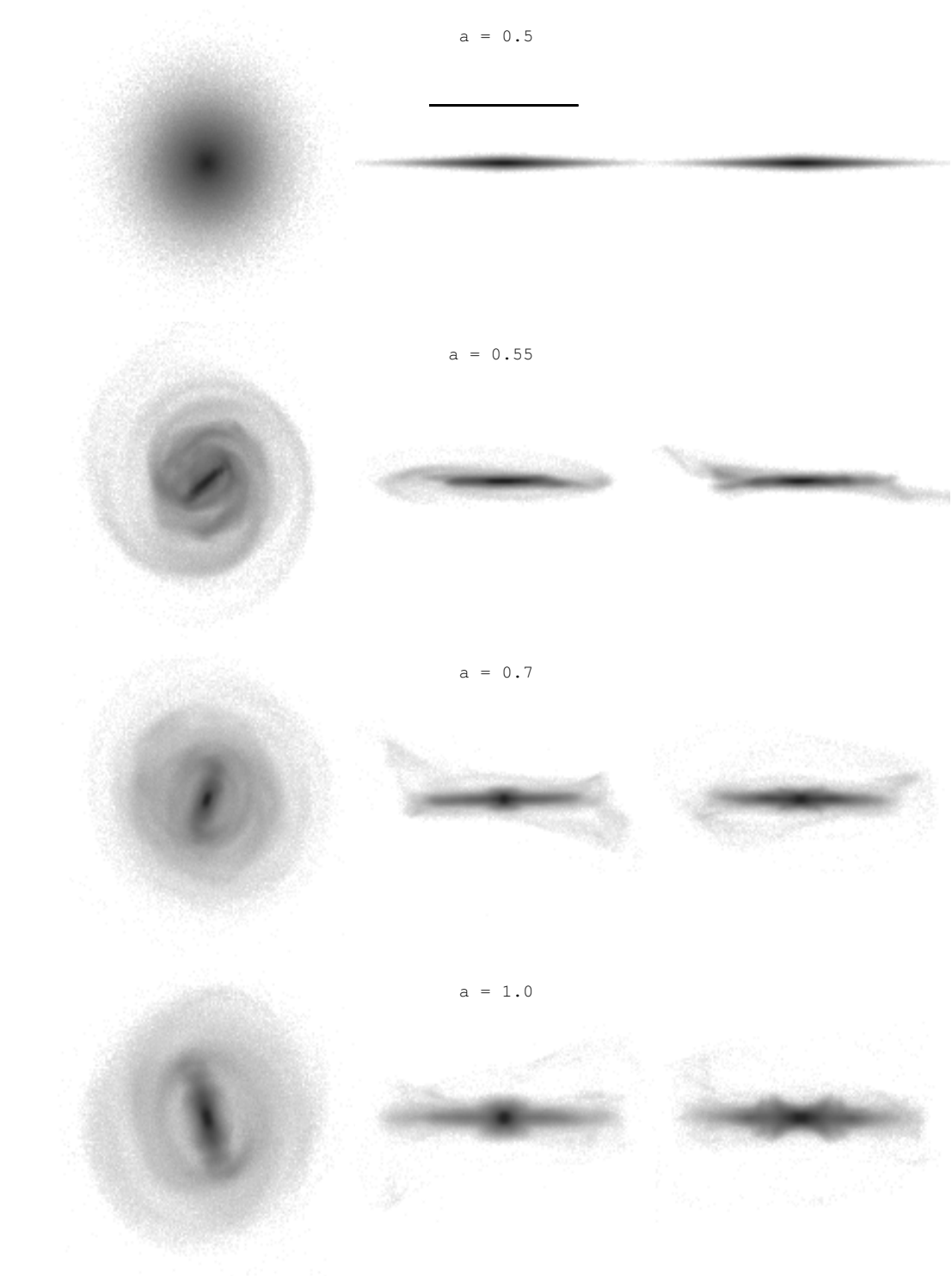


Figure 3.6: Projected density along three orthogonal directions for the live disc at four epochs between  $z = 1$  and  $z = 0$ . The projections are presented in physical units. The solid line for scale is 37 kpc with a centre coincident with the disc's.

### 3.4.1 Bar Formation

In Fig. 3.6 we show orthogonal projections of the disc density in our LD simulation at four epochs between  $z = 1$  (lookback time of 7.9 Gyr) and the present epoch. During the first billion years of live disc evolution, the disc develops a bar and spiral structure. In addition, there is a warp in the outer disc extending several kiloparsecs above the midplane of the inner disc. By the present epoch, the bar has grown in length and intensified and the edge-on view shows the classic X-pattern.

We consider the usual parameter bar strength  $A_2 = |c_2|$  where

$$c_m = \frac{1}{M_S} \sum_{j \in S} m_j e^{im\phi_j} . \quad (3.11)$$

Here,  $S$  is some circularly-symmetric region of the disc (e.g., a circular annulus) and the sum is over all particles labeled by  $j$  and with mass  $m_j$  that are inside  $S$ . We find that  $A_2$  for the inner  $2R_d$  of the disc reaches 0.43 at  $t = 6.7$  Gyr, decreases to 0.36 by  $t = 9.2$  Gyr, presumably because the bar has buckled, and then increases to 0.47 by the present epoch. On the other hand,  $A_2$  for the entire disc increases to 0.27, decreases to 0.23, and then increases to 0.28 for the same epochs. Note that the inner  $2R_d$  of the disc contains 60% of the mass. Thus, the fact that  $A_{2,2R_d}/A_{2,\text{tot}} \simeq 0.6$  implies that most of the bar mass resides within the inner  $2R_d$ .

The bars in Yurin and Springel (2015) seem to be stronger than the ones in our simulations — they find  $A_2 \simeq 0.6$  but use a non-standard formula for  $A_2$ . Moreover, their bars appear to extend across most of the disc. In terms of disc dynamics, the main difference between our simulations is the fact that we use a three-integral DF for the disc whereas they use a two-integral DF. In the latter, the velocity dispersion in the radial and vertical directions are the same. Thus, the radial dispersion, which

fixes the Toomre  $Q$  parameter, also determines the thickness of the disc. We note that their initial discs are a factor of two or three thicker than ours. We speculate that the bars that develop in these thick discs are less susceptible to buckling and therefore able to grow stronger and longer. These ideas will be investigated in more detail in a future publication.

### 3.4.2 Kicked-up Stars and Disc Heating

The outer part of the disc suffers considerable disruption and warping presumably through its interaction with the main halo or substructure. The right-most panel of the  $a = 0.55$  snapshot in Fig. 3.6, for example, shows a classic integral-sign warp. The other snapshots show that a significant number of disc particles have orbits that now take them to high galactic latitudes.

The impressions one has from the density projections are borne out in Fig. 3.7 where we show the surface density and scale height profiles at different times. Bar formation redistributes mass in the disc leaving a deficit (relative to the initial exponential disk) between 5 and 15 kpc. The disc becomes thicker and its vertical velocity dispersion increases through a combination of disc-halo interactions and the effects of the bar and spiral structure (Gauthier et al., 2006; Dubinski et al., 2008; Kazantzidis et al., 2008).

A striking feature of the simulations are the streams of disc stars well above the disc plane. These stars may represent an example of a kicked-up disc, which has been seen in other N-body simulations (Purcell et al., 2010; McCarthy et al., 2012) and invoked to explain kinematic and spectroscopic observations of M31 (Dorman et al., 2013) and the Monoceros Ring (e.g. Newberg et al., 2002; Ibata et al., 2003).

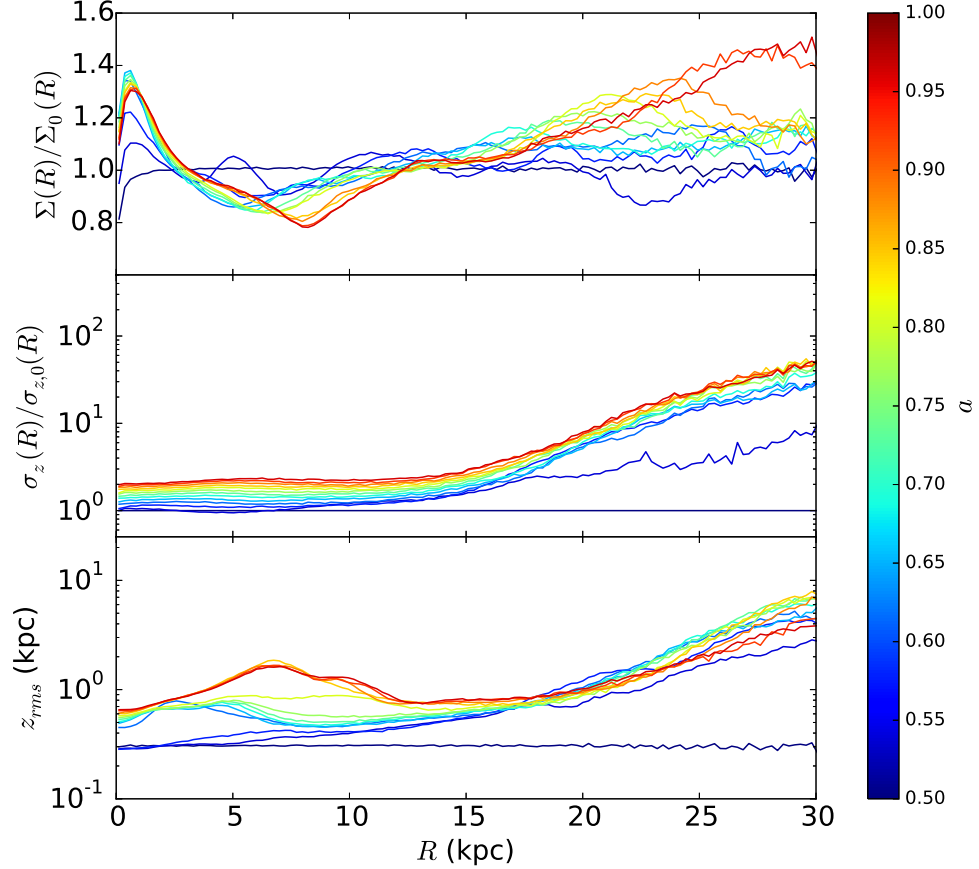


Figure 3.7: Surface density, vertical velocity dispersion, and scale height profiles of the live disc for 10 snapshots equally spaced in scale factor  $a$  between  $a = 0.5$  ( $z = 1$ ) and  $a = 1$  (present epoch). Panels are the same as in Fig. 3.3.

The idea is that interactions between the disc and both satellite galaxies and halo substructure liberate stars from the disc, launching them to regions of the galaxy normally associated with the stellar halo. Our live disc simulation corroborates this hypothesis and is in broad agreement with previous numerical work.

Finally, we note that the  $a = 1$  panel of Fig. 3.6 shows a relatively thin, stream-like structure, above the disc which is qualitatively similar to the Anti-centre Stream (ACS, Grillmair, 2006). While the ACS is believed to be due to the disruption of a globular cluster (e.g. Grillmair, 2006), Fig. 3.6 suggests that perturbations to the disc can create similar features. Intriguingly, (de Boer et al., 2017) recently found that the ACS is rotating in the same sense as the Milky Way disc.

### 3.5 Halo Substructure in the Presence of a Disc

In this section, we consider the effect of a disc on a halo’s structural properties such as its spherically-averaged density profile, its shape, and its subhalo population. An examination of the DMO simulation shows that the halo we have selected builds up through a series of mergers and accretion events, but that by  $z = 1$  it has settled into a relatively relaxed state with an NFW profile that evolves very little between  $z = 1$  and  $z = 0$  within the inner 100 kpc. Our sequence of simulations, (MN, FO, RD, and LD) allow us to tease out the effects of different disc insertion methods. The MN simulation, for example, pins the centre of the disc to the minimum of the halo potential, whereas the other simulations dynamically evolve the position and velocity of the disc potential via Newtonian mechanics. The MN and FO simulations both assume that the orientation of the disc potential during the growth phase is fixed whereas RD and LD solve for the orientation using rigid body dynamics.

#### 3.5.1 Global Properties of the Halo

In Fig. 3.8 we show the ratio of the spherically-averaged density profile in the four disc runs to that from the DMO run. At  $z = 1$  the haloes in the FO, RD, and MN

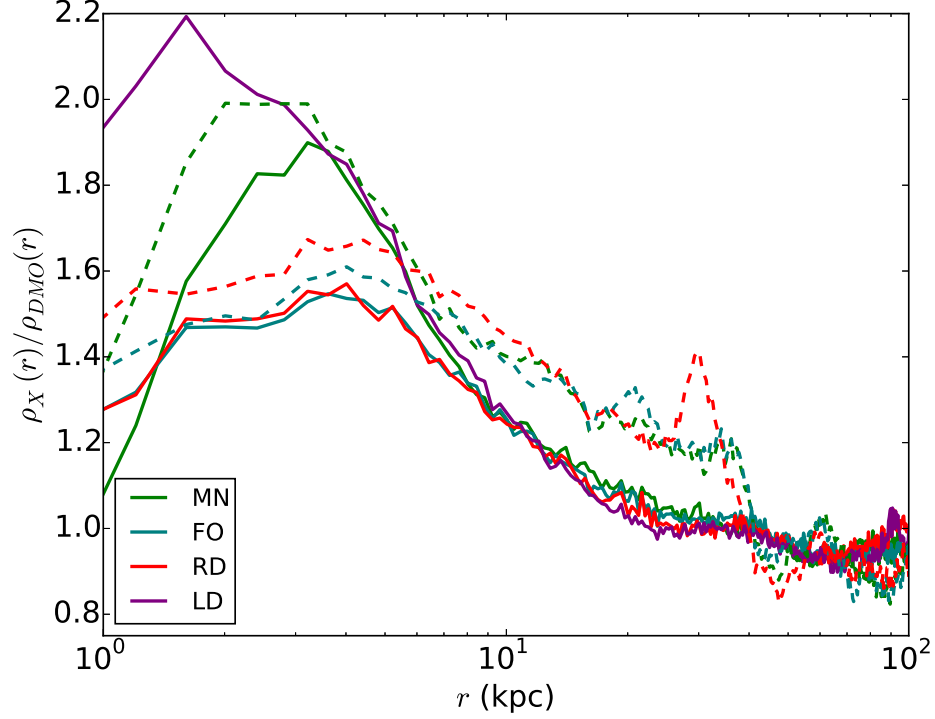


Figure 3.8: The ratio of halo density to the DMO simulation for MN (green), FO (teal), RD (red), and LD (purple) at  $z = 1$  (dashed) and  $z = 0$  (solid). The presence of the disc significantly increases the central concentration of the halo.

runs show evidence for adiabatic contraction with the density in the inner  $\sim 30$  kpc increasing by a factor of  $1.2 - 2.1$ . The effect is strongest in the MN simulation, which is to be expected since the halo in that case always sees the disc potential at the minimum of its potential. Of course, this prescription is unphysical. In general, and especially during a major merger, the disc and halo potential minimum will not necessarily coincide.

Between  $z = 1$  and  $z = 0$ , the mass of the disc is constant. Adiabatic contraction ceases but the halo still responds to the time-varying disc potential. Interestingly, at intermediate radii (between  $\sim 10 - 40$  kpc) the density profile of the halo settles

back to a state close to that found in the DMO run. Perhaps most striking is the fact that the halo in the LD run becomes more centrally concentrated than the halo in any of the other cases. One possible explanation is that dynamical friction from the disc drags dark matter subhaloes toward the centre of the halo where they are tidally disrupted.

In Fig. 3.9 we show the minor-to-major ( $c_r/a_r$ ) and intermediate-to-major ( $b_r/a_r$ ) axis ratios as a function of radius for both the  $z = 1$  and  $z = 0$  snapshots. The axis ratios are calculated by diagonalizing the moment of inertia tensor in linearly-spaced radial shells. The DMO halo is triaxial with  $c_r/a_r \simeq 0.75$  and  $b_r/a_r \simeq 0.85$ . Note that the axis ratio profiles are smoother at  $z = 0$  than at  $z = 1$ , which supports the observation that the halo has settled into a more relaxed state over the past 7 or so billion years. In general, discs tend to make halos more spherical, a result that has been known for some time from both collisionless and hydrodynamical simulations (e.g. Dubinski, 1994; Zemp et al., 2012).

Evidently, the MN halo is rounder, especially in the inner part, than the FO halo. Recall that the main difference between these two cases is that the MN disc is pinned to the potential minimum of the halo. It is perhaps not surprising then that, as with adiabatic contraction, it has a stronger effect on the halo's shape. We also note that the axis ratio profiles for the RD and LD simulations are fairly similar.

### 3.5.2 Subhalo Populations

We now turn our attention to halo substructure. We identify subhaloes and determine their positions and masses using ROCKSTAR (Behroozi et al., 2013), which employs a friends-of-friends algorithm in six phase space dimensions. We consider only those



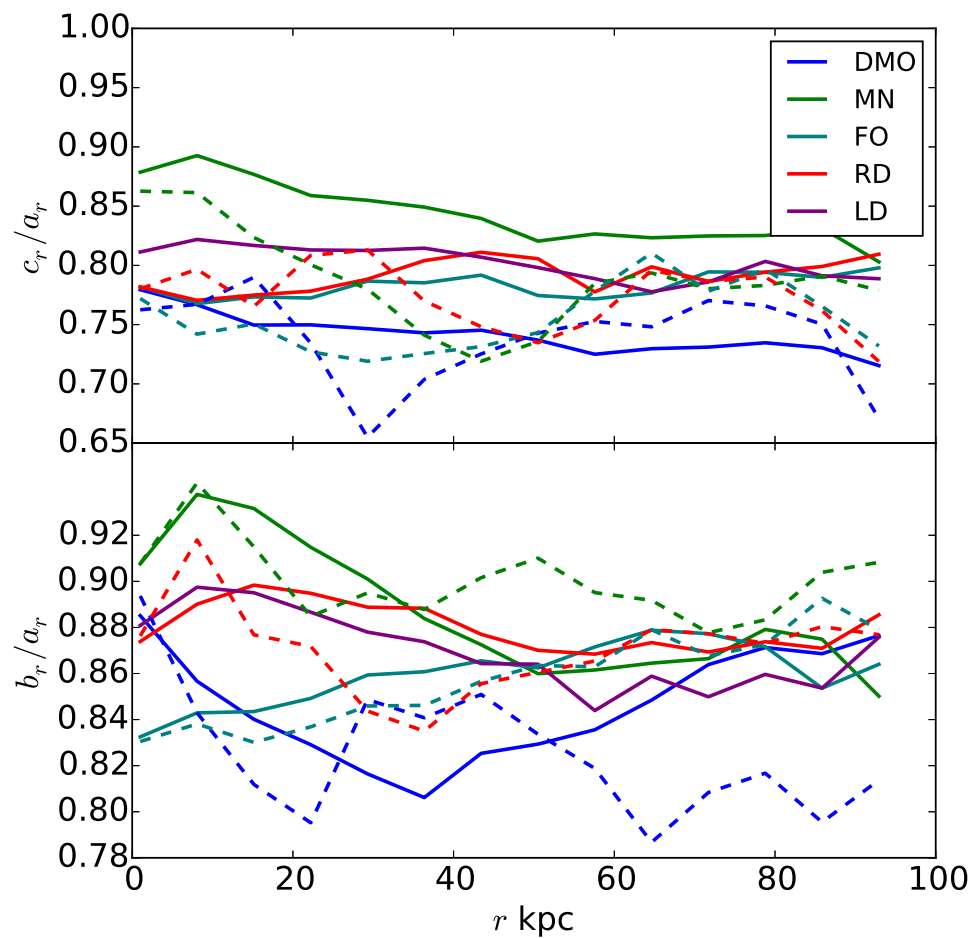


Figure 3.9: Axis ratios as a function of radius. Shown are the minor-to-major axis ratio (top panel) and the intermediate-to-major axis ratio (bottom panel) at  $z = 1$  (dashed curves) and  $z = 0$  (solid curves). Blue corresponds to DMO, green to MN, teal to FO, red to RD, and purple to LD.

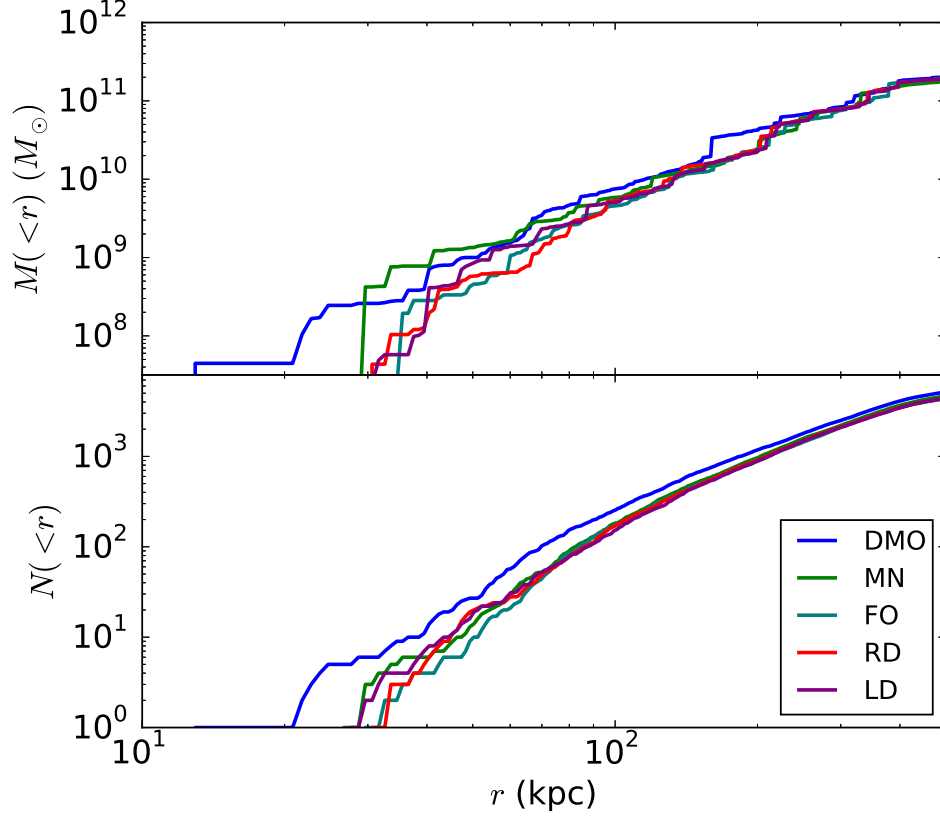


Figure 3.10: Cumulative mass in subhaloes inside a radius  $r$  (upper panel) and cumulative number of subhaloes (lower panel). We consider only subhaloes within 500 kpc of the halo centre and with a mass above  $10^{7.5} M_{\odot}$ . The curves are blue (DMO), green (MN), teal (FO), red (RD), and purple (LD).

subhaloes with mass  $m_s$  between  $m_{\min} = 10^{7.5} M_{\odot}$  and  $m_{\max} = 10^{10.5} M_{\odot}$ . Subhaloes at the lower end of this range are marginally resolved with  $\sim 100$  particles, above which the subhalo mass can be trusted (e.g. Onions et al., 2012), while those at the upper end contain  $\sim 3\%$  of the halo’s virial mass.

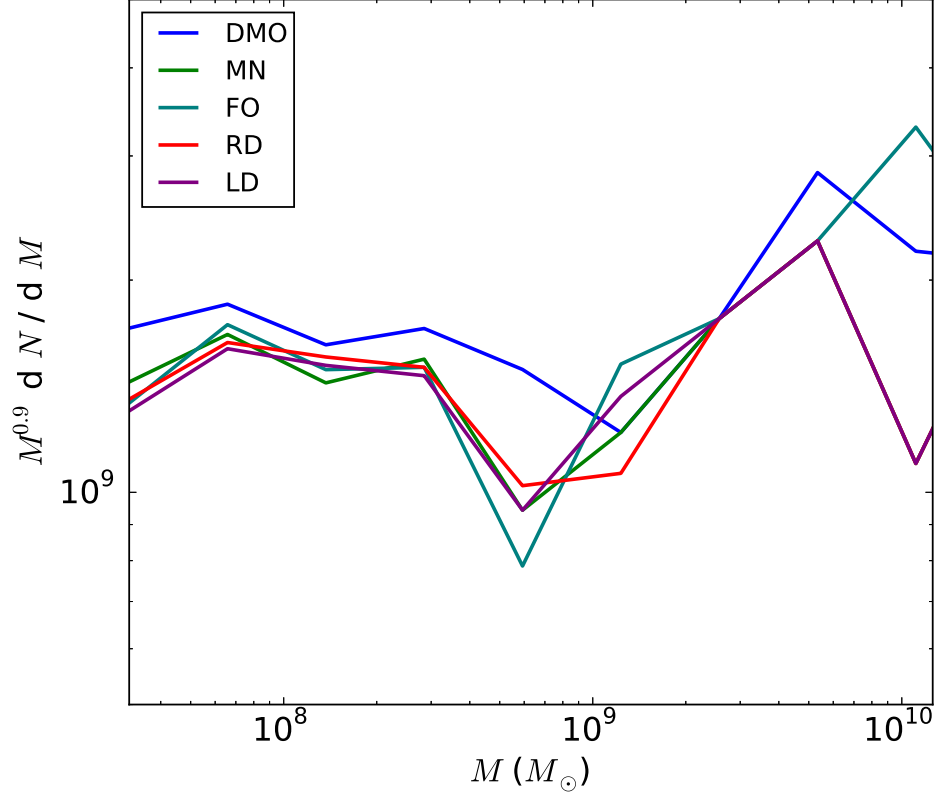


Figure 3.11: Differential mass distribution multiplied by  $M^{0.9}$  for subhaloes above  $10^{7.5} M_{\odot}$ . We make an outer radius cut at 500 kpc. The curves are blue (DMO), green (MN), teal (FO), red (RD), and purple (LD).

In Fig. 3.10 we show the cumulative mass in subhaloes as a function of Galactocentric radius:

$$M_s(< r) = \int_0^r dr \int_{m_{\min}}^{m_{\max}} dm_s m_s \frac{d^2 N}{dm_s dr} \quad (3.12)$$

We also show the cumulative number of subhaloes. In general, the presence of a disc depletes substructure inside about 30 kpc but leaves the outer substructures unaffected.

We next consider the differential mass distribution as a function of subhalo mass. Recall that for a pure dark matter halo,  $dN/d\ln(m_s) \propto m_s^{-p}$  where  $p \simeq 0.9$  (e.g. Gao et al., 2004). In Fig. 3.11, we therefore show the quantity  $m^{0.9} dN/d\ln(m_s)$  in order to enhance the differences between the different disc runs. We see that the halo population between  $m_s \simeq m_{\min}$  and  $m_s \simeq 10^9 M_\odot$  is depleted, but only by about 20 – 30 %. Taken together, Fig. 3.10 and Fig. 3.11 imply that the main depletion of the subhaloes occurs within the inner regions of the parent halo, in agreement with D’Onghia et al. (2010); Sawala et al. (2017); Garrison-Kimmel et al. (2017). That said, the depletion of subhaloes seems rather insensitive to the disc insertion method, although we caution that only a single halo was used. Our results, being mainly in agreement with previous work, should still be viewed with caution due the consideration of a single host halo.

### 3.5.3 Case Study: A Sagittarius-like Dwarf

Observations of the Milky Way’s dwarf galaxies and associated tidal streams provide a potentially powerful probe of the Galactic potential and thus the Galaxy’s dark halo. One of the best-studied examples is the Sagittarius dwarf Ibata et al. (1994). Fortunately, our simulation has a satellite galaxy with similar properties, namely, a dark matter mass of  $1.8 \times 10^{10} M_\odot$  at  $z = 1.0$  and an orbit that takes it close to the disc. We identify this object in the five simulations using the ROCKSTAR halo catalogues. We then gather a list of IDs for all the bound particles at an early time before the dwarf is disrupted and follow these same particles in later snapshots using a binary search tree look-up scheme. In Fig. 3.12 we show the evolution of this subhalo between redshift  $z_l = 1$  and  $z = 0$ . The first row shows the baseline evolution in our

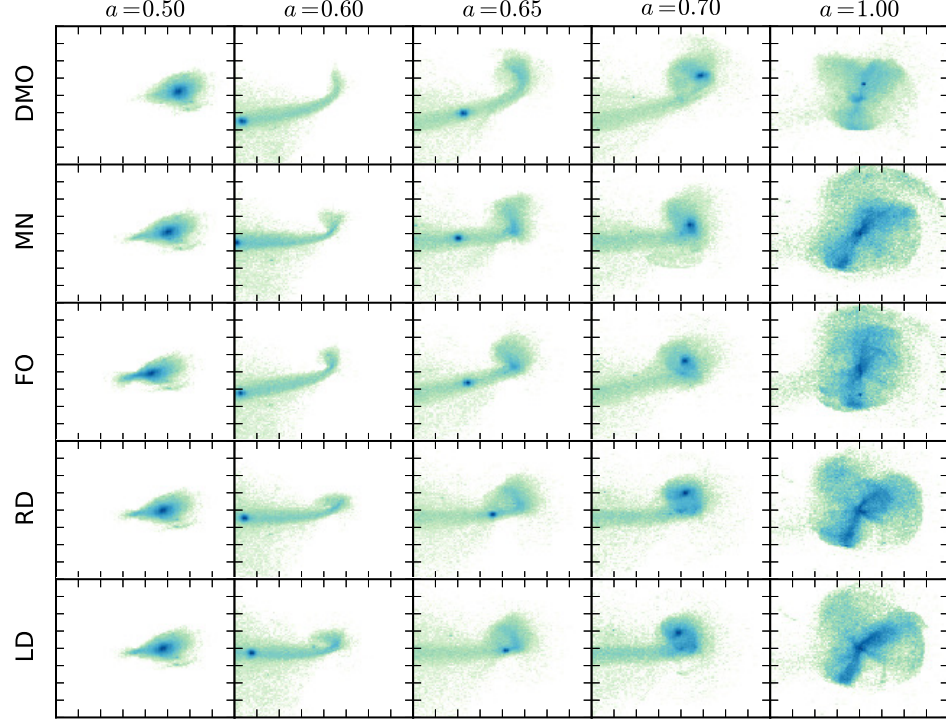


Figure 3.12: X-Y projections for a selected Sagittarius-like dwarf galaxy. The rows from top to bottom are no disc, a fixed Miyamoto-Nagai disc, a rigid disc, and a live disc. The scale factors in columns from left to right are 0.5, 0.55, 0.6, 0.65, and 0.7. The frame edges are 295 kpc on each side.

DMO simulation. The dwarf develops leading and trailing tidal tails during the first few billion years. By the present epoch, the tidal debris has dispersed throughout the halo.

The next four rows show the same satellite in our disc simulations. Perhaps the most noticeable result is that there are stronger features in the tidal debris at the present epoch once a disc is included. The detailed morphology of the tidal debris is certainly different from one disc simulation to the next. By eye, debris in MN

and FO look somewhat similar as does the debris in RD and LD. Perhaps the most noticeable result is that the tidal debris extends to larger galactocentric radii when a disc is included. The detailed morphology of the tidal debris clearly depends on the disc insertion method. By eye, tidal debris appears more isotropic in MN and FO than in RD and LD. The implication is that fixed potentials are more efficient at disrupting massive satellites than a potential which can respond to the satellite's presence. However, we have only a single example of massive satellite disruption, and we caution that more examples of this behaviour are needed to test this hypothesis.

### 3.6 Conclusions

Simulations in which a stellar disc is inserted “by hand” into a cosmological N-body halo provide a compromise between simulations of isolated disc-halo systems and cosmological simulations that include gasdynamics and star formation. Our method builds on the scheme used by Berentzen and Shlosman (2006); DeBuhr et al. (2012) and refined by Yurin and Springel (2015). The basic idea is to introduce, at a redshift  $z_g$ , a rigid disc with zero mass into a halo within a cosmological zoom-in simulation. Between  $z_g$  and  $z_l$  the disc is treated as an external potential with a mass and size that increase adiabatically to their present day values. At  $z_l$ , the rigid disc is replaced by an N-body one and the simulation proceeds to the present epoch with live disc and halo particles.

Our method improves upon previous ones in two important ways. First, during the growth phase ( $z_g > z > z_l$ ) the position and orientation of the disc evolve according to the standard equations of rigid-body dynamics. Thus, the disc in our scheme receives its linear and angular momentum with the halo in a self-consistent fashion

and is therefore able to move, precess, and nutate due to torques from the halo. While previous methods introduced aspects of rigid-body dynamics during the growth phase none appear to have implemented the full dynamical equations have done here (D’Onghia et al., 2010; DeBuhr et al., 2012; Yurin and Springel, 2015).

Our sequence MN, FO, RD, and LD of simulations highlights where the details of the disc insertion scheme are important and where they are not. For example, schemes in which the disc tracks the minimum of the halo potential tend to overestimate the effects of adiabatic contraction. On the other hand, the effect of the depletion of halo substructure seems to be rather insensitive to the details of how the disc is introduced into the simulation.

Disc insertion schemes such as the one introduced in this paper, provide an attractive arena for studies of galactic dynamics. In particular, they allow one to study the interaction between a stellar disc and a realistic dark halo with computationally inexpensive simulations while maintaining some level of control over the structural parameters of the disc. We fully intend to leverage these advantages in future work.

## Bibliography

- Behroozi, P. S., Wechsler, R. H., and Wu, H.-Y. (2013). The ROCKSTAR Phase-space Temporal Halo Finder and the Velocity Offsets of Cluster Cores. *ApJ*, 762:109.
- Berentzen, I. and Shlosman, I. (2006). Growing Live Disks within Cosmologically Assembling Asymmetric Halos: Washing Out the Halo Prolateness. *ApJ*, 648:807–819.
- Binney, J. and Tremaine, S. (2008). *Galactic Dynamics: Second Edition*. Princeton University Press.
- de Boer, T. J. L., Belokurov, V., and Koposov, S. E. (2017). The fall of the Northern Unicorn: Tangential motions in the Galactic Anti-centre with SDSS and Gaia. *ArXiv e-prints*.
- DeBuhr, J., Ma, C.-P., and White, S. D. M. (2012). Stellar discs in Aquarius dark matter haloes. *MNRAS*, 426:983–999.
- D’Onghia, E., Springel, V., Hernquist, L., and Keres, D. (2010). Substructure Depletion in the Milky Way Halo by the Disk. *ApJ*, 709:1138–1147.
- Dorman, C. E., Widrow, L. M., Guhathakurta, P., Seth, A. C., Foreman-Mackey, D., Bell, E. F., Dalcanton, J. J., Gilbert, K. M., Skillman, E. D., and Williams,



- B. F. (2013). A New Approach to Detailed Structural Decomposition from the SPLASH and PHAT Surveys: Kicked-up Disk Stars in the Andromeda Galaxy? *ApJ*, 779:103.
- Dubinski, J. (1994). The effect of dissipation on the shapes of dark halos. *ApJ*, 431:617–624.
- Dubinski, J., Gauthier, J.-R., Widrow, L., and Nickerson, S. (2008). Spiral and Bar Instabilities Provoked by Dark Matter Satellites. In Funes, J. G. and Corsini, E. M., editors, *Formation and Evolution of Galaxy Disks*, volume 396 of *Astronomical Society of the Pacific Conference Series*, page 321.
- Dubinski, J. and Kuijken, K. (1995). The settling of warped disks in oblate dark halos. *ApJ*, 442:492–503.
- Font, A. S., Navarro, J. F., Stadel, J., and Quinn, T. (2001). Halo Substructure and Disk Heating in a  $\Lambda$  Cold Dark Matter Universe. *ApJ*, 563:L1–L4.
- Gao, L., White, S. D. M., Jenkins, A., Stoehr, F., and Springel, V. (2004). The subhalo populations of  $\Lambda$ CDM dark haloes. *MNRAS*, 355:819–834.
- Garrison-Kimmel, S., Wetzel, A. R., Bullock, J. S., Hopkins, P. F., Boylan-Kolchin, M., Faucher-Giguere, C.-A., Keres, D., Quataert, E., Sanderson, R. E., Graus, A. S., and Kelley, T. (2017). Not so lumpy after all: modeling the depletion of dark matter subhalos by Milky Way-like galaxies. *ArXiv e-prints*.
- Gauthier, J.-R., Dubinski, J., and Widrow, L. M. (2006). Substructure around M31: Evolution and Effects. *ApJ*, 653:1180–1193.

- Gómez, F. A., White, S. D. M., Grand, R. J. J., Marinacci, F., Springel, V., and Pakmor, R. (2016). Warps and waves in fully cosmological models of galactic discs. *ArXiv e-prints*.
- Grillmair, C. J. (2006). Substructure in Tidal Streams: Tributaries in the Anticenter Stream. *ApJ*, 651:L29–L32.
- Hahn, O. and Abel, T. (2013). MUSIC: MUlti-Scale Initial Conditions. Astrophysics Source Code Library.
- Hu, S. and Sijacki, D. (2016). Stellar spiral structures in triaxial dark matter haloes. *MNRAS*, 461:2789–2808.
- Ibata, R. A., Gilmore, G., and Irwin, M. J. (1994). A dwarf satellite galaxy in Sagittarius. *Nature*, 370:194–196.
- Ibata, R. A., Irwin, M. J., Lewis, G. F., Ferguson, A. M. N., and Tanvir, N. (2003). One ring to encompass them all: a giant stellar structure that surrounds the Galaxy. *MNRAS*, 340:L21–L27.
- Katz, N., Quinn, T., Bertschinger, E., and Gelb, J. M. (1994). Formation of Quasars at High Redshift. *MNRAS*, 270:L71.
- Katz, N., Weinberg, D. H., and Hernquist, L. (1996). Cosmological Simulations with TreeSPH. *ApJS*, 105:19.
- Kazantzidis, S., Bullock, J. S., Zentner, A. R., Kravtsov, A. V., and Moustakas, L. A. (2008). Cold Dark Matter Substructure and Galactic Disks. I. Morphological Signatures of Hierarchical Satellite Accretion. *ApJ*, 688:254–276.

- Klypin, A., Kravtsov, A. V., Valenzuela, O., and Prada, F. (1999). Where Are the Missing Galactic Satellites? *ApJ*, 522:82–92.
- Kuijken, K. and Gilmore, G. (1989). The mass distribution in the galactic disc. I - A technique to determine the integral surface mass density of the disc near the sun. *MNRAS*, 239:571–603.
- Laporte, C. F. P., Gómez, F. A., Besla, G., Johnston, K. V., and Garavito-Camargo, N. (2016). Response of the Milky Way’s disc to the Large Magellanic Cloud in a first infall scenario. *ArXiv e-prints*.
- McCarthy, I. G., Font, A. S., Crain, R. A., Deason, A. J., Schaye, J., and Theuns, T. (2012). Global structure and kinematics of stellar haloes in cosmological hydrodynamic simulations. *MNRAS*, 420:2245–2262.
- Miyamoto, M. and Nagai, R. (1975). Three-dimensional models for the distribution of mass in galaxies. *PASJ*, 27:533–543.
- Moore, B., Ghigna, S., Governato, F., Lake, G., Quinn, T., Stadel, J., and Tozzi, P. (1999). Dark Matter Substructure within Galactic Halos. *ApJ*, 524:L19–L22.
- Navarro, J. F., Frenk, C. S., and White, S. D. M. (1994). Accretion of Satellite Galaxies and the Density of the Universe. *MNRAS*, 267:L1.
- Navarro, J. F., Frenk, C. S., and White, S. D. M. (1997). A Universal Density Profile from Hierarchical Clustering. *ApJ*, 490:493–508.
- Newberg, H. J., Yanny, B., Rockosi, C., Grebel, E. K., Rix, H.-W., Brinkmann, J., Csabai, I., Hennessy, G., Hindsley, R. B., Ibata, R., Ivezić, Z., Lamb, D., Nash,

- E. T., Odenkirchen, M., Rave, H. A., Schneider, D. P., Smith, J. A., Stolte, A., and York, D. G. (2002). The Ghost of Sagittarius and Lumps in the Halo of the Milky Way. *ApJ*, 569:245–274.
- Oñorbe, J., Garrison-Kimmel, S., Maller, A. H., Bullock, J. S., Rocha, M., and Hahn, O. (2014). How to zoom: bias, contamination and Lagrange volumes in multimass cosmological simulations. *MNRAS*, 437:1894–1908.
- Onions, J., Knebe, A., Pearce, F. R., Muldrew, S. I., Lux, H., Knollmann, S. R., Ascasibar, Y., Behroozi, P., Elahi, P., Han, J., Maciejewski, M., Merchán, M. E., Neyrinck, M., Ruiz, A. N., Sgró, M. A., Springel, V., and Tweed, D. (2012). Subhaloes going Notts: the subhalo-finder comparison project. *MNRAS*, 423:1200–1214.
- Pakmor, R. and Springel, V. (2013). Simulations of magnetic fields in isolated disc galaxies. *MNRAS*, 432:176–193.
- Planck Collaboration, Ade, P. A. R., Aghanim, N., Armitage-Caplan, C., Arnaud, M., Ashdown, M., Atrio-Barandela, F., Aumont, J., Baccigalupi, C., Banday, A. J., and et al. (2014). Planck 2013 results. XVI. Cosmological parameters. *A&A*, 571:A16.
- Power, C., Navarro, J. F., Jenkins, A., Frenk, C. S., White, S. D. M., Springel, V., Stadel, J., and Quinn, T. (2003). The inner structure of  $\Lambda$ CDM haloes - I. A numerical convergence study. *MNRAS*, 338:14–34.
- Purcell, C. W., Bullock, J. S., and Kazantzidis, S. (2010). Heated disc stars in the stellar halo. *MNRAS*, 404:1711–1718.

- Purcell, C. W., Bullock, J. S., Tollerud, E. J., Rocha, M., and Chakrabarti, S. (2011). The Sagittarius impact as an architect of spirality and outer rings in the Milky Way. *Nature*, 477:301–303.
- Roškar, R., Debattista, V. P., Brooks, A. M., Quinn, T. R., Brook, C. B., Governato, F., Dalcanton, J. J., and Wadsley, J. (2010). Misaligned angular momentum in hydrodynamic cosmological simulations: warps, outer discs and thick discs. *MNRAS*, 408:783–796.
- Sackett, P. D. (1997). Does the Milky Way Have a Maximal Disk? *ApJ*, 483:103–110.
- Sawala, T., Pihajoki, P., Johansson, P. H., Frenk, C. S., Navarro, J. F., Oman, K. A., and White, S. D. M. (2017). Shaken and stirred: the Milky Way’s dark substructures. *MNRAS*, 467:4383–4400.
- Schaye, J., Crain, R. A., Bower, R. G., Furlong, M., Schaller, M., Theuns, T., Dalla Vecchia, C., Frenk, C. S., McCarthy, I. G., Helly, J. C., Jenkins, A., Rosas-Guevara, Y. M., White, S. D. M., Baes, M., Booth, C. M., Camps, P., Navarro, J. F., Qu, Y., Rahmati, A., Sawala, T., Thomas, P. A., and Trayford, J. (2015). The EAGLE project: simulating the evolution and assembly of galaxies and their environments. *MNRAS*, 446:521–554.
- Sellwood, J. A. (2013). *Dynamics of Disks and Warps*, page 923. Springer.
- Springel, V. (2005). The cosmological simulation code GADGET-2. *MNRAS*, 364:1105–1134.
- Springel, V. and Hernquist, L. (2003). Cosmological smoothed particle hydrodynamics simulations: a hybrid multiphase model for star formation. *MNRAS*, 339:289–311.

- Springel, V., Wang, J., Vogelsberger, M., Ludlow, A., Jenkins, A., Helmi, A., Navarro, J. F., Frenk, C. S., and White, S. D. M. (2008). The Aquarius Project: the subhaloes of galactic haloes. *MNRAS*, 391:1685–1711.
- Stinson, G., Seth, A., Katz, N., Wadsley, J., Governato, F., and Quinn, T. (2006). Star formation and feedback in smoothed particle hydrodynamic simulations - I. Isolated galaxies. *MNRAS*, 373:1074–1090.
- Thornton, S. T. and Marion, J. B. (2008). *"Classical Dynamics of Particles and Systems"*. "Cengage Learning", 5 edition.
- Torres-Flores, S., Epinat, B., Amram, P., Plana, H., and Mendes de Oliveira, C. (2011). GHASP: an H $\alpha$  kinematic survey of spiral and irregular galaxies - IX. The near-infrared, stellar and baryonic Tully-Fisher relations. *MNRAS*, 416:1936–1948.
- van Dokkum, P. G., Leja, J., Nelson, E. J., Patel, S., Skelton, R. E., Momcheva, I., Brammer, G., Whitaker, K. E., Lundgren, B., Fumagalli, M., Conroy, C., Förster Schreiber, N., Franx, M., Kriek, M., Labbé, I., Marchesini, D., Rix, H.-W., van der Wel, A., and Wuyts, S. (2013). The Assembly of Milky-Way-like Galaxies Since  $z \sim 2.5$ . *ApJ*, 771:L35.
- Vogelsberger, M., Genel, S., Sijacki, D., Torrey, P., Springel, V., and Hernquist, L. (2013). A model for cosmological simulations of galaxy formation physics. *MNRAS*, 436:3031–3067.
- Widrow, L. M., Pym, B., and Dubinski, J. (2008). Dynamical Blueprints for Galaxies. *ApJ*, 679:1239–1259.

- Yurin, D. and Springel, V. (2014). GALIC: Galaxy initial conditions construction. Astrophysics Source Code Library.
- Yurin, D. and Springel, V. (2015). The stability of stellar discs in Milky Way-sized dark matter haloes. *MNRAS*, 452:2367–2387.
- Zemp, M., Gnedin, O. Y., Gnedin, N. Y., and Kravtsov, A. V. (2012). The Impact of Baryon Physics on the Structure of High-redshift Galaxies. *ApJ*, 748:54.

## Chapter 4

### Cosmological Bar Formation: Nature vs Nurture

#### 4.1 Abstract

We investigate the connection between the vertical structure of stellar discs and the formation of bars using high-resolution simulations of galaxies in isolation and in the cosmological context. In particular, we simulate a suite of isolated galaxy models that have the same Toomre  $Q$  parameter and swing amplification parameter but that differ in the vertical scale height and velocity dispersion. We find that the onset of bar formation occurs more slowly in models with thicker discs. Moreover, thicker discs and also discs evolved in simulations with larger force softening also appear to be more resilient to buckling, which acts to regulate the length and strength of bars. We also simulate disc-halo systems in the cosmological environment using a disc-insertion technique developed in a previous paper. In this case, bar formation is driven by the stochastic effects of a triaxial halo and subhalo-disc interactions and the initial growth of bars appears to be relatively insensitive to the thickness of the disc. On the other hand, thin discs in cosmological halos do appear to be more susceptible to buckling than thick ones and therefore bar strength correlates with disc thickness as in the



isolated case. More to the point, one can form discs in cosmological simulations with relatively weak bars or no bars at all provided the discs as thin as the discs we observe and the softening length is smaller than the disc scale height.

## 4.2 Introduction

The problem of bar formation in disc galaxies tests our understanding of cosmological structure formation and galactic dynamics. In principle, theories of galaxy formation should yield predictions for the fractional distribution of bars in terms of their strength, length, and pattern speed. While it is often difficult to make precise, quantitative statements about bars from observations, general properties of their distribution have emerged (See Sellwood and Wilkinson (1993), Sellwood (2013) and Binney and Tremaine (2008) for reviews). Roughly 30-40 per cent of disc galaxies exhibit strong bars, that is bars that dominate the disc luminosity. Another 20 per cent or more have relatively weak bars. The bar fraction appears to increase with time. Approximately one tenth of disc galaxies between  $0.5 \leq z \leq 2$  have visually identifiable strong bars, which is a factor of 3-4 smaller than the fraction in the local Universe (see Simmons et al. (2014) and references therein). The bar fraction also varies with galaxy type. Masters et al. (2010) find that  $70 \pm 5$  per cent of the so-called passive red spirals have bars as compared to a  $25 \pm 5$  per cent bar fraction for blue spirals. Since the red spirals are interpreted as old galaxies that have used up their star-forming gas, this result is consistent with a bar fraction that increases with time. The upshot of these observations is that in terms of bars, disc galaxies in the local Universe divide into three roughly equal bins: those with strong bars, those with weak bars, and those with no detectable bar. These observations suggest that bars

are capable of forming at a wide range of cosmic times, but once formed, are difficult to destroy.

Intuition tells us that properties of a bar should depend on the properties of its host galaxy and the environment in which that galaxy lives. Theoretical arguments indicate that cold, thin discs are susceptible to local “Toomre” instabilities. Furthermore, discs that are strongly self-gravitating, that is discs that contribute the bulk of the gravitational force required to maintain their rotational motion, are susceptible to global instabilities. Thus, one can construct initially axisymmetric galaxy models that form bars with vastly different properties (or no bars at all) by changing the internal disc dynamics or trading off disc mass for bulge and halo mass. The implication is that the distribution of bars provides an indirect means for inferring a disc’s kinematics and mass-to-light ratio as well as the distribution of mass in a galaxy’s dynamically “hot” components, namely its bulge and dark matter halo.

A galaxy’s ability to resist local instabilities is typically expressed in terms of the (kinetic) Toomre  $Q$ -parameter (Toomre, 1964) while its ability to resist global instabilities is encapsulated in the swing-amplification  $X$ -parameter (Goldreich and Tremaine, 1978, 1979). Both parameters are defined so that large values imply a more stable disc. The hypothesis that they determine a galaxy’s susceptibility to bar formation has been tested by simulations of isolated, idealized galaxy models (Ostriker and Peebles, 1973; Zang and Hohl, 1978; Combes and Sanders, 1981; Sellwood, 1981). Typically, the initial galaxy is represented by an N-body (Monte Carlo) realization of an equilibrium solution to the collisionless Boltzmann equation comprising a disc, dark matter halo, and often, a bulge. Equilibrium does not imply stability, and a galaxy can develop spiral structure and a bar through instabilities that are seeded by shot noise

(Efsthathiou et al., 1982) and amplified by feedback loops such as swing amplification (Sellwood, 2013). A common way to suppress the mechanisms which give rise to these effects is by increasing either  $Q$  or  $X$ . For example, in dynamically warm discs (that is, discs with high  $Q$ ) perturbations are randomized on timescales short enough to prevent the feedback loop from starting (Athanasoula and Sellwood, 1986). Likewise, submaximal discs, that is, discs with high  $X$ , avoid the bar instability presumably because the disc lacks the self-gravity to drive the bar instability (Efsthathiou et al., 1982; Christodoulou et al., 1995; Sellwood, 2013).

As one might imagine, the parameters  $Q$  and  $X$  do not uniquely describe a galaxy’s susceptibility to bar formation. Widrow et al. (2008) present a grid of models in the  $Q - X$  plane that all satisfy observational constraints for the Milky Way. These simulations confirm the basic notion that susceptibility to instabilities increases with decreasing  $Q$  and  $X$ . However, a careful study of bar strength and length as a function of time across these simulations suggests a more complicated picture. In particular, the bar strength is not a perfectly monotonic function of  $X$  at fixed  $Q$  or vice versa. The implication is that additional parameters are required to fully predict how bar formation will proceed from some prescribed initial conditions. In short, bar formation may proceed very differently within a family of models that have the same  $Q$  and  $X$  but vary in other ways.

One property of a disc not captured by either  $Q$  or  $X$  is its thickness, or alternatively, its vertical velocity dispersion. (The Toomre parameter depends only on the radial velocity dispersion.) Klypin et al. (2009) use a suite of simulations to demonstrate that the thickness of the disc plays a profound role in the development of a bar. In particular, their thick disc model forms a stronger and more slowly rotating

bar as compared with the bar that forms in a thin disc model with the same initial radial dispersion profile and rotation curve decomposition. Moreover, simulation parameters such as mass resolution and time step also influence the growth of the bar instability and slowdown of the bar due to angular momentum transfer with the dark halo (Dubinski et al., 2009).

Of course, galaxies are neither isolated nor born as axisymmetric, equilibrium systems. In these idealized systems, instabilities can only come from shot noise, whereas this is not true in a complicated dynamical environment. As such, bar formation may be very different in idealized galaxies as compared with galaxies in a cosmological setting. For example, halo substructure in the form of satellite galaxies and dark matter subhaloes can pass through and perturb the disc. Gauthier et al. (2006), Kazantzidis et al. (2008), and Dubinski et al. (2009) showed that an apparently stable disc galaxy model can develop a bar when a fraction of the “smooth” halo is replaced by substructure in the form of subhaloes. The effect is stochastic; subhalo-triggered bar formation seems to require subhaloes whose orbits take them into the central regions of the disc in a prograde sense. More recently, Purcell et al. (2011) showed that Sagittarius dwarf alone could have been responsible for the Milky Way’s spiral structure and bar.

Cosmological haloes also possess large-scale time-dependent tidal fields, which impart torques to the disc and cause it to precess, nutate, and warp (Dubinski and Kuijken, 1995a; Binney et al., 1998; Dubinski and Chakrabarty, 2009; Bauer et al., 2018). In turn, stellar discs can reshape the inner parts of the dark matter haloes via adiabatic contraction and dynamical friction (Blumenthal et al., 1986; Ryden and Gunn, 1987; Dubinski, 1994; Dubinski and Kuijken, 1995b; DeBuhr et al., 2012;

Yurin and Springel, 2015; Bauer et al., 2018). In principle, one can turn to *ab initio* hydrodynamic cosmological simulations to capture the effects of both triaxiality and substructure. Indeed, galaxy formation studies in the cosmological environment that include the formation of supermassive black holes, stars, and the feedback from these objects on galaxy formation have had remarkable success over the last decade (See, for example Vogelsberger et al. (2013); Schaye et al. (2015)). Unfortunately, feedback techniques are extremely computationally expensive. Moreover, the simulator cannot control the properties of the disc such as its mass and radial scale length that form within a particular haloes. This restriction makes it difficult to explore the “nature vs. nurture” question: Do bars reflect the structure of their host galaxy, substructure interactions of the disc’s lifetime, or large-scale tidal fields from the dark halo?

Techniques developed by Berentzen and Shlosman (2006), DeBuhr et al. (2012), Yurin and Springel (2015), Bauer et al. (2018) and others allow one to insert a collisionless disc into a dark matter halo. These techniques provide a compromise between fully cosmological simulations and simulations of isolated galaxies. In general, the first step is to run a pure dark matter simulation of a cosmological volume and select a halo suitable for the galaxy one intends to study. The simulation is then rerun with a rigid disc potential that is adiabatically grown from some early epoch (say redshift  $z = 3$ ) and an intermediate one (say  $z = 1$ ). Doing so allows the halo to respond to “disc formation”. At the intermediate redshift, a suitable N-body disc that is approximately in equilibrium is swapped in for the rigid disc potential and the simulation continues, now with live disc and halo particles.

Perhaps the most striking and perplexing result to come from recent disc-insertion simulations is the prevalence of strong bars. Yurin and Springel (2015), for example,

find that all of the discs in their bulge-less simulations for strong bars even though some of these discs are decidedly submaximal. In addition, over half of the discs in simulations with classical bulges form strong bars. Their results suggest that discs in the cosmological setting are more prone to forming strong bars and that bulges play an essential role in explaining the presence of disc galaxies with weak bars or no bars at all.

Though the Yurin and Springel (2015) models vary in  $Q$  and  $X$  they share two important properties. First, the ratio of the radial and vertical velocity dispersion is set to unity throughout the disc. Second, the ratio of the vertical and radial scale lengths is fixed at 0.2, which is roughly a factor of two larger than that of the Milky Way's thin disc. In addition, the softening length in their simulations is fixed at 680 pc. Thus, the discs in their simulations are thicker and (vertically) warmer than what one might expect for Milky Way-like galaxies. The results from Klypin et al. (2009) suggest that these properties rather than (or together with) halo substructure and triaxiality are responsible for the preponderance of strong bars in the Yurin and Springel (2015) models.

In this paper, we attempt to isolate the different effects that determine whether a galaxy forms a strong bar, a weak one, or no bar at all. The core of the paper is a sequence of N-body simulations that include simulations of isolating disc galaxies and galaxies in cosmological haloes. Our choice of models is meant to complement those of Yurin and Springel (2015). In particular, we choose models that have the same  $Q$  and  $X$  but that vary in their vertical structure.

We begin in section §4.3 by discussing the dimensionless parameters that arise

when one constructs equilibrium disc galaxy models. These include the aforementioned  $Q$  and  $X$  parameters as well as the ratio of the vertical and radial velocity dispersion and the ratio of the vertical and radial scale lengths. We also discuss possible effects of gravitational softening. In 4.4 we describe our sequence of simulations and discuss how they fit in with previous work. We discuss results for our isolated galaxy simulations in §4.5 and our cosmological ones in §4.6. We conclude with a discussion of the implications of our results in §4.7.

### 4.3 Theoretical Considerations

In this section, we consider the structural properties of disc-halo models with an eye toward understanding the formation of bars in these systems. We begin with the  $Q$  and  $X$  parameters and then discuss the vertical structure of the disc as defined by its scale height, vertical velocity dispersion, and surface density. Finally, we consider the effect softening might have on bar formation.

#### 4.3.1 $Q$ and $X$

The stability of a stellar disc is generally thought to be determined by the Toomre- $Q$  parameter (Toomre, 1964)

$$Q \equiv \frac{\sigma_R \kappa}{3.36 G \Sigma} \quad (4.1)$$

and the Goldreich-Tremaine (swing amplification) parameter (Goldreich and Tremaine, 1978, 1979)

$$X_m \equiv \frac{\kappa^2 R}{2\pi m G \Sigma} \quad (4.2)$$

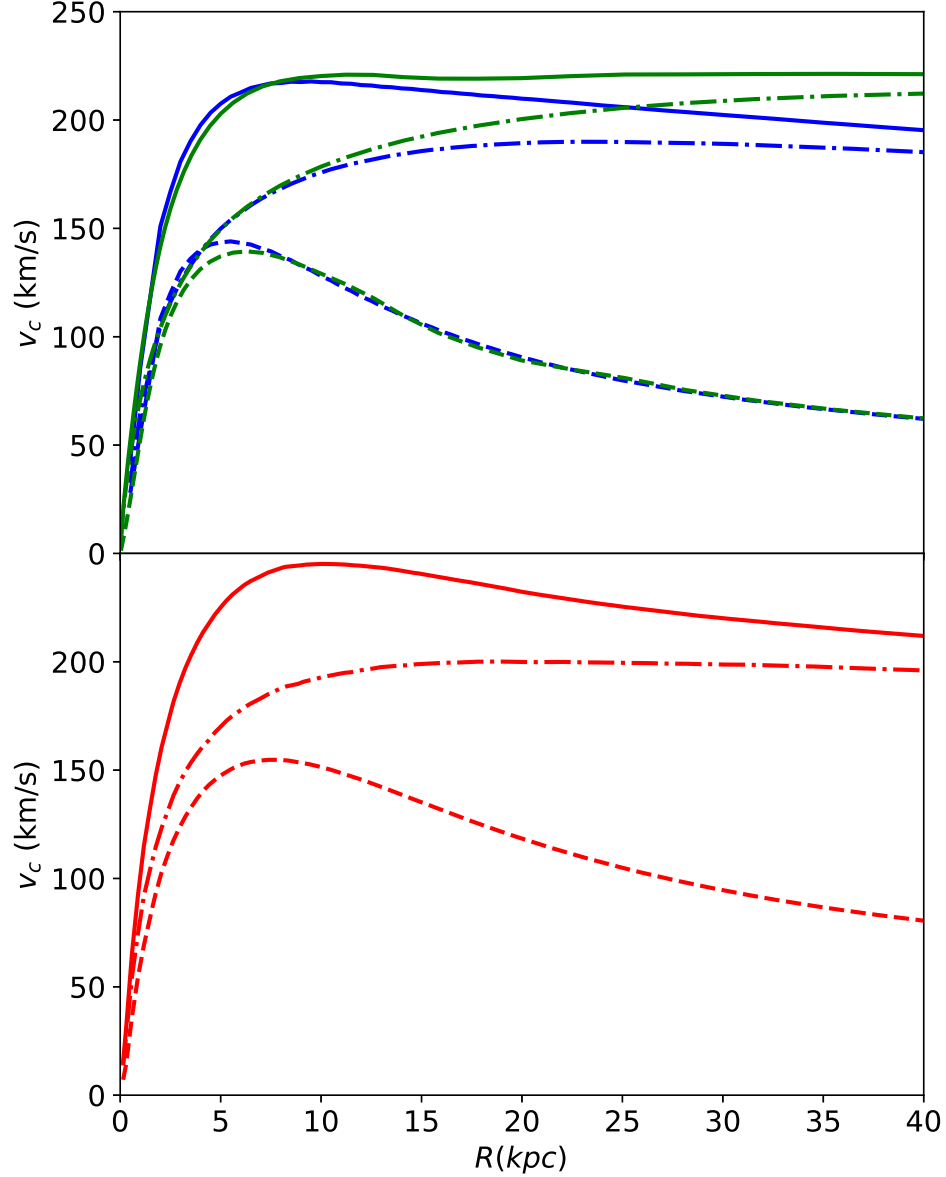


Figure 4.1: Rotation curve decomposition for our models. Total rotation curves are shown as solid lines while the separate contributions from the disc and halo are shown as dashed and dot-dashed curves, respectively. Blue curves in the top panel are for the isolated galaxy simulations with GALACTICS initial conditions while the green curves are for the simulations C.I.Ag run with AGAMA initial conditions. Bottom panel shows initial rotation curve decomposition for the runs D.I and E.II.



	$M_d$	$R_d$	$V_c$	$\sigma_R$	$z_d/R_d$	$\sigma_R/\sigma_z$	$X$	$Q$	$\rho_h/\rho_0$	$\epsilon$
A.I	3.49	2.50	216	25.3	0.10	1.27	2.34	1.00	0.14	0.15
A.II	3.49	2.50	216	25.3	0.10	1.27	2.34	1.00	0.14	0.50
B.I	3.49	2.50	213	25.3	0.20	0.97	2.34	1.00	0.28	0.15
B.II	3.49	2.50	213	25.3	0.20	0.97	2.34	1.00	0.28	0.50
C.I	3.49	2.50	208	25.3	0.40	0.77	2.34	1.00	0.50	0.15
C.I.Ag	3.49	2.50	216	25.3	0.40	0.77	2.34	1.00	0.50	0.15
D.IV	5.82	3.70	245	25.2	0.10	1.14	2.45	1.00	0.29	0.18
E.IV	5.82	3.70	245	27.4	0.25	0.72	2.45	1.00	0.73	0.74
YS15.A5	5.00	3.00	263	30.7	0.2	1.00	3.22	1.38	0.21	0.68
YS15.B5	5.00	3.00	211	26.6	0.2	1.00	2.06	0.96	0.11	0.68
YS15.C5	5.00	3.00	270	30.3	0.2	1.00	3.31	1.42	0.23	0.68
YS15.D5	5.00	3.00	236	26.6	0.2	1.00	2.58	1.12	0.16	0.68
YS15.E5	5.00	3.00	233	27.1	0.2	1.00	2.58	1.11	0.15	0.68
YS15.F5	5.00	3.00	219	27.0	0.2	1.00	2.22	1.02	0.11	0.68
YS15.G5	5.00	3.00	227	28.2	0.2	1.00	2.45	1.09	0.13	0.68
YS15.H5	5.00	3.00	244	28.6	0.2	1.00	2.85	1.21	0.16	0.68
G06	7.77	5.57	226	17.1	0.06	1.80	2.78	1.43	0.10	0.15

Table 4.1: Summary of parameters for the simulations considered in this paper, the disk-halo simulations considered in Yurin and Springel (2015) (labeled YS15) and the Gauthier et al. (2006) (G06).  $M_d$  is the final disc mass in units of  $10^{10} M_\odot$ ,  $R_d$  is the disc scale radius in units of kpc, and  $V_c$  and  $\sigma_R$  are the circular speed and radial velocity dispersion in units of  $\text{km s}^{-1}$  and evaluated at  $R_p = 2.2R_d$ . For the disc aspect ratio, we quote  $z_d/R_d$  where  $z_d$  is the  $\text{sech}^2$ -scale length. The velocity dispersion ratio  $\sigma_R/\sigma_z$ , the  $X$  and  $Q$  parameters, the ratio of the halo density in the midplane to that of the disc, and the logarithmic derivative of the circular speed are also measured at  $R_p$ . Finally, the softening length  $\epsilon$  is given in units of kpc. Simulations A.III and B.III are the same as A.I and B.I except that they are run with vertical motions isotropized so as to shut off the buckling instability.

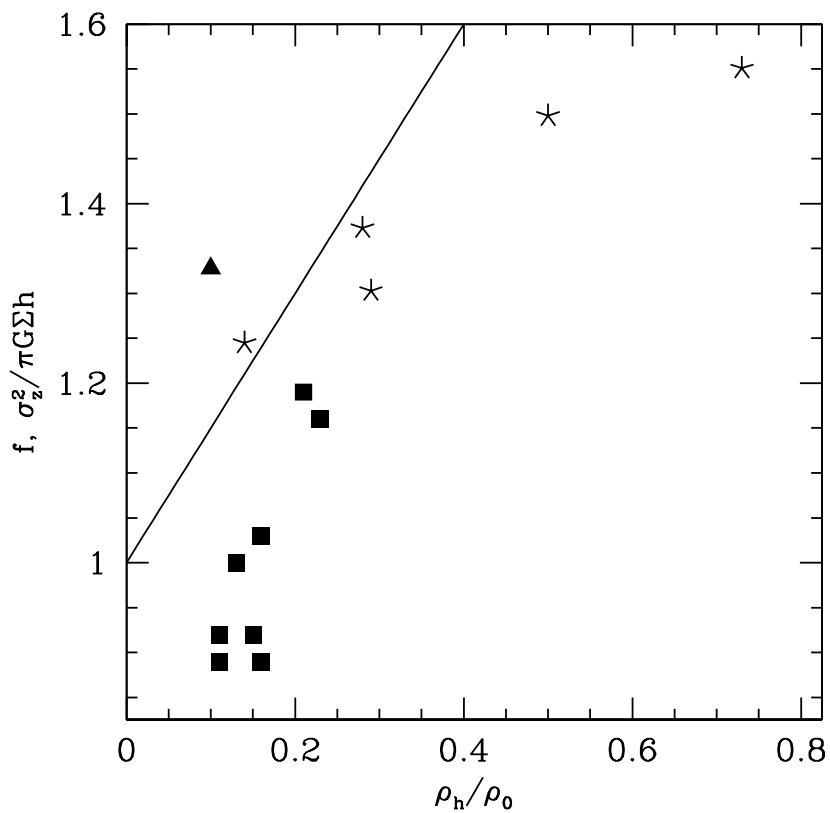


Figure 4.2: The dimensionless ratio  $\sigma_z^2 / \pi G \Sigma z_d$  as a function of  $\rho_h / \rho_0$  for the models considered in this paper (stars), the disc-halo models from Yurin and Springel (2015) (filled squares) and the model from Gauthier et al. (2006) (filled triangle). The straight line is the function  $f = 1 + (2\pi/3)^{1/2} \rho_h / \rho_0$  discussed in the text.

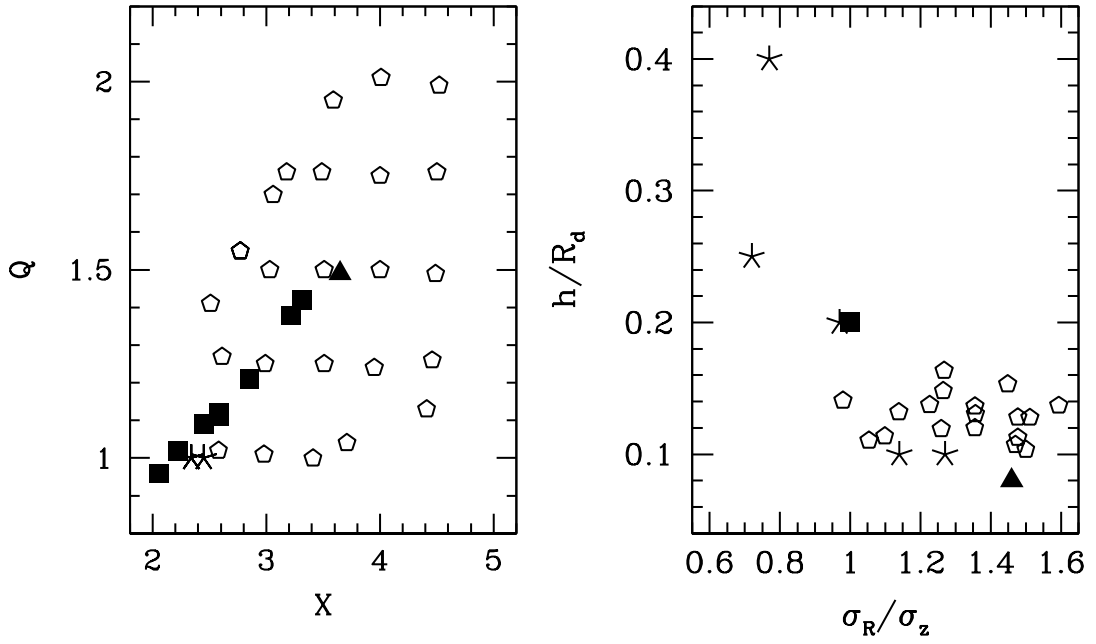


Figure 4.3: Distribution of simulations considered in this paper in the  $Q - X$  and the  $z_d/R_d - \sigma_R/\sigma_z$  planes. Stars are simulations run for this paper (A-E); filled squares denote the series of simulations described in Yurin and Springel (2015); the filled triangle denotes the simulation of M31 run in Gauthier et al. (2006); open pentagons denote the simulations described in Widrow et al. (2008).

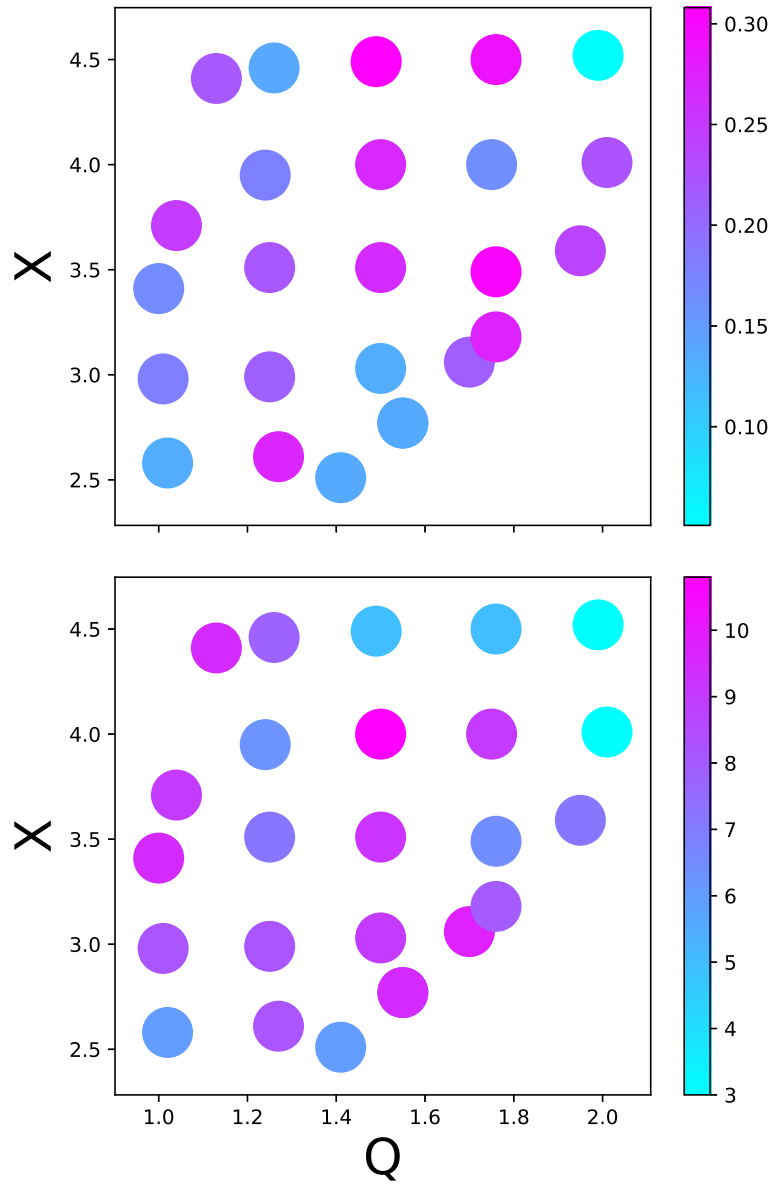


Figure 4.4: Strength and length of bars for the simulations considered in Gauthier et al. (2006). The twenty-five models span the  $Q$ - $X$  plane. Top panel shows the  $A_2$  parameter while the bottom panel shows the bar length. Both are measured at 5 Gyr (the final snapshot of the simulations).

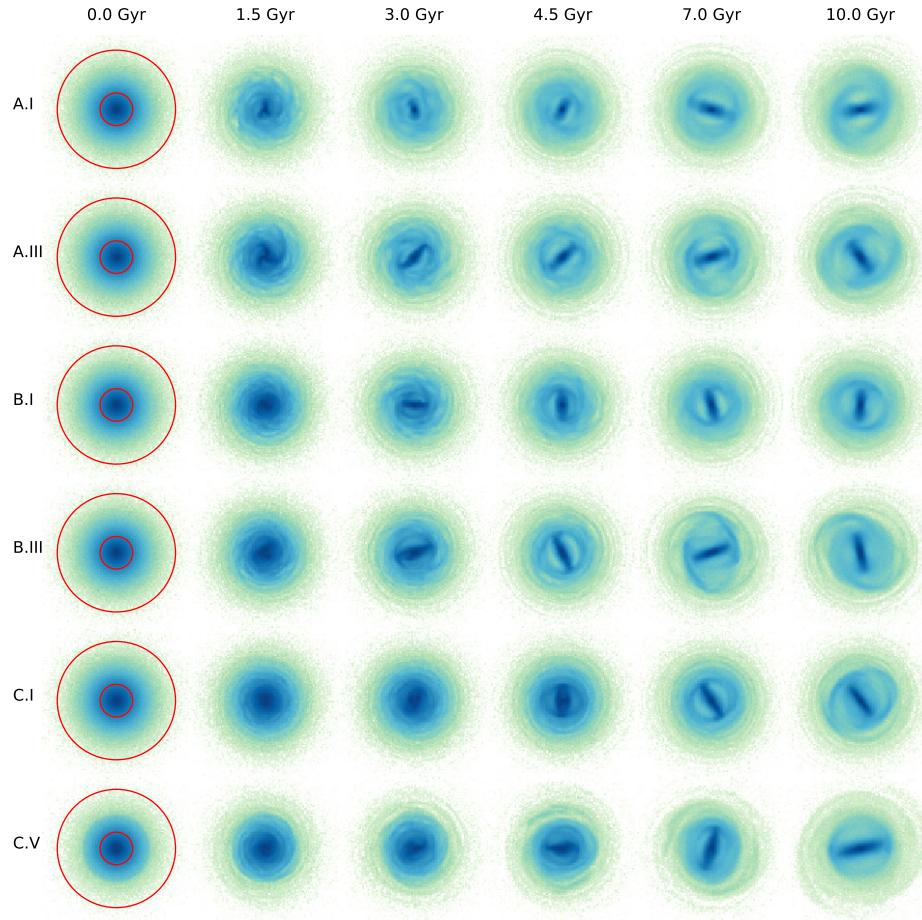


Figure 4.5: Surface density maps for isolated galaxy simulations at select times. Time proceeds from 0 to 10 Gyr, left-to-right, and the models span top-to-bottom in order of their appearance in Table 4.1. The overlaid red circles have radii  $R_p = 5.5$  kpc and 20 kpc.

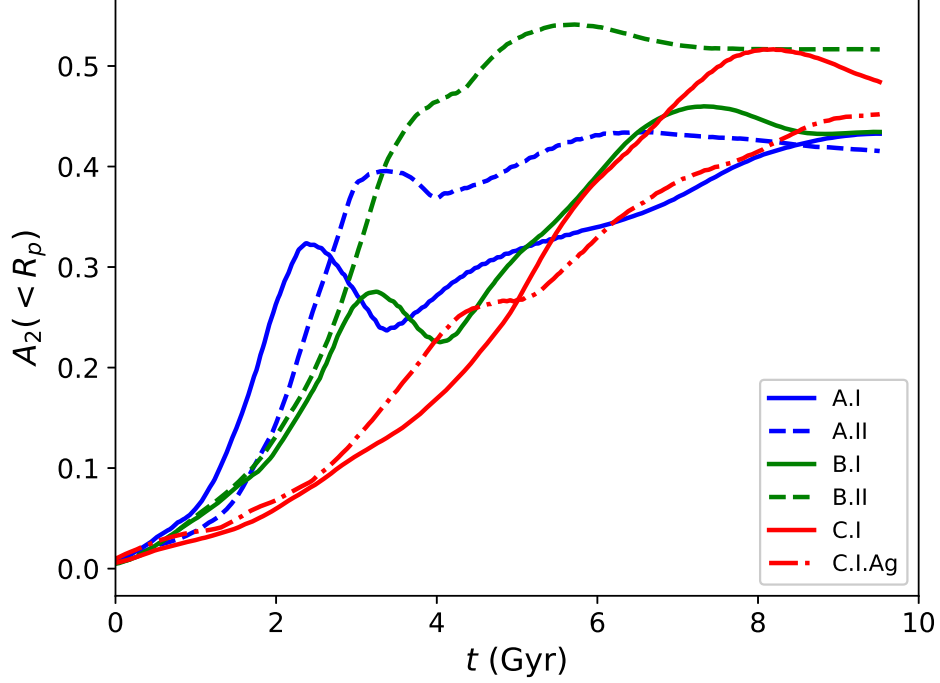


Figure 4.6: Mean bar strength parameter inside a cylindrical radius  $R_p$ ,  $A_2(< R_p)$ , as a function of time. Curves are smoothed in time with a top-hat moving window of width 1 Gyr. Line colors are blue, red, and green for models A, B, and C, respectively. Results for the fiducial runs A.I, B.I, and C.I are shown as solid curves while the results for the runs with high softening length, A.II and B.II, are shown as dashed curves. The AGAMA model C.I.Ag is shown as a dot-dashed curve.

where  $R$  is the Galactocentric radius of a cylindrical  $(R, \phi, z)$  coordinate system,  $\Sigma$  is the surface density of the disc,  $\sigma_R$  is the radial velocity dispersion of the disc, and  $m$  is the azimuthal mode number. The epicyclic radial frequency  $\kappa$  is given by

$$\kappa^2 = \frac{2V_c^2}{R^2} \left( 1 + \frac{d \ln V_c}{d \ln R} \right) \quad (4.3)$$

where  $V_c$  is the circular speed. We assume an exponential disc with mass  $M_d$ , radial

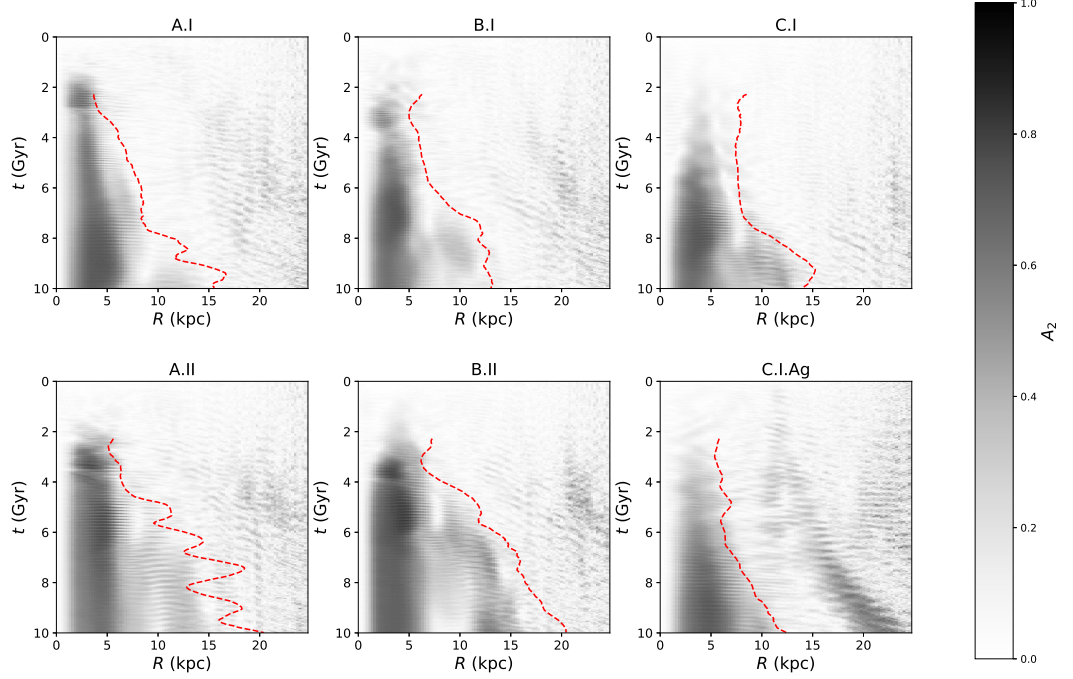


Figure 4.7: Bar strength parameter  $A_2$  as a function of radius and time. The trajectory of corotation is shown by the dashed red line.

scale length  $R_d$ , and surface density

$$\Sigma(R) = \frac{M_d}{2\pi R_d^2} e^{-R/R_d} . \quad (4.4)$$

Note that  $\kappa$ ,  $\sigma_R$ ,  $\Sigma$ ,  $V_c$ ,  $Q$ , and  $X_m$  are functions of  $R$ . In what follows, we consider the radius  $R_p$  at which the contribution to the rotation curve from the disc,  $V_d$  reaches a peak value. For an exponential disc,  $R_p \simeq 2.2R_d$  and  $V_d(R_p) \simeq 0.62 (GM_d/R_d)^{1/2}$  (Binney and Tremaine, 2008).

Roughly speaking,  $Q$  describes the susceptibility of a disc to local instabilities.

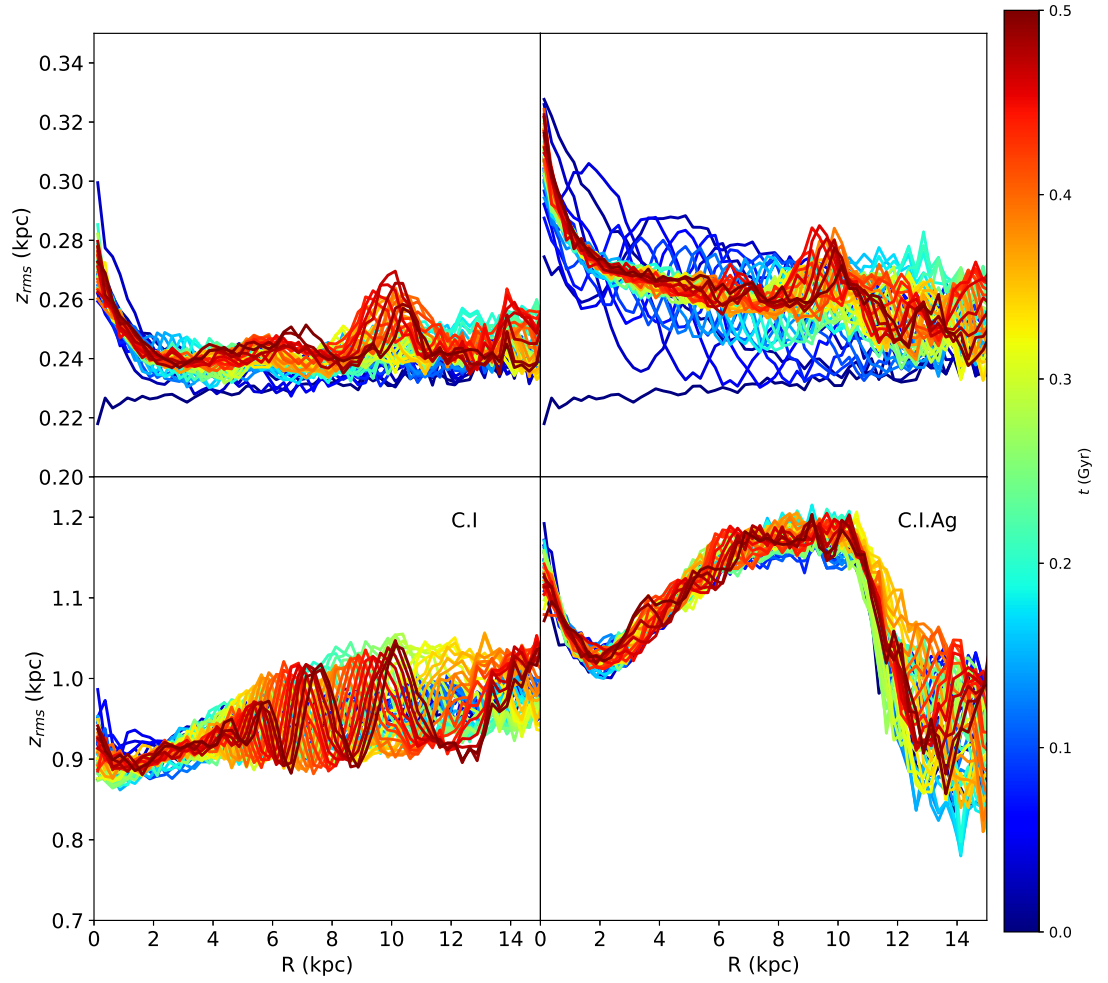


Figure 4.8: Root mean square height  $z_{rms}$  as a function of cylindrical radius  $R$  for ten snapshots equally spaced over the first 500 Myr. Panels are for simulations A.I (upper left), A.II (upper right), C.I (lower left) and C.I.Ag (lower right).



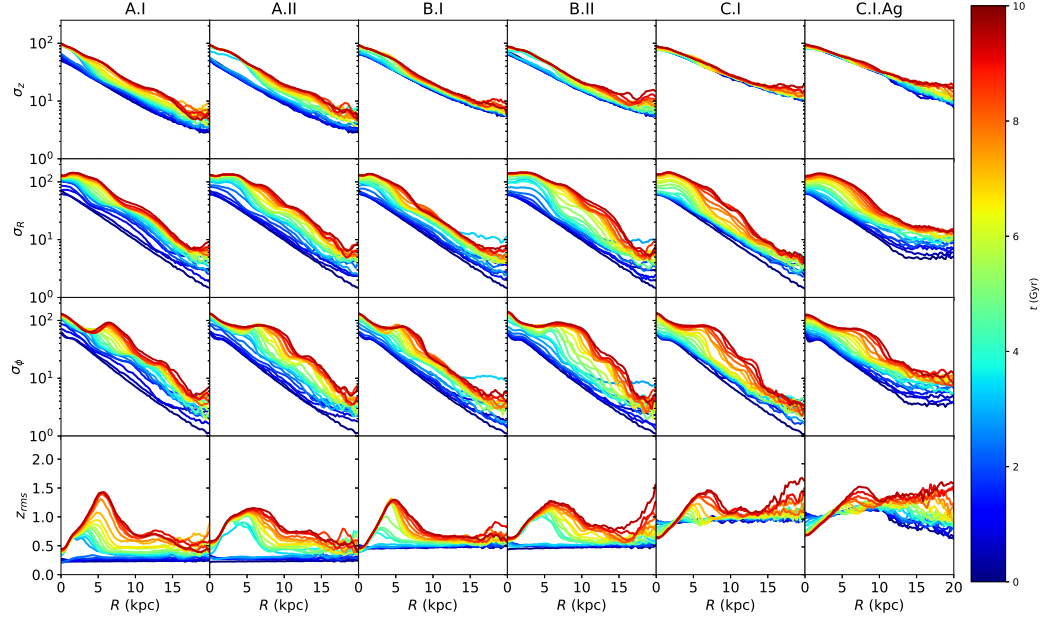


Figure 4.9: Diagonal components of the velocity dispersion tensor and  $z_{\text{rms}}$  as a function of  $R$  for different snapshots between 0 and 10 Gyr. Shown, from top to bottom, are profiles for  $z_{\text{rms}}$ ,  $\sigma_z$ ,  $\sigma_R$ , and  $\sigma_\phi$  for the same size models included in Fig. 4.5.

Cold discs with low velocity dispersion and  $Q < 1$  are unstable to local perturbations. On the other hand,  $X_m$  describes the vigour with which a global perturbation with an  $m$ -fold azimuthal symmetry undergoes swing amplification. Since we are interested in bar formation, we set  $m = 2$  and note that  $X_2^{-1}$  is a measure of disc self-gravity. To see this, we use Eq. (4) and the expression for  $V_{d,p}$  to find

$$X_2(R_p) \simeq 0.79 \left. \frac{V_c^2}{V_d^2} \right|_{R_p} \quad (4.5)$$

where we have assumed that the logarithmic derivative in Eq.(4.3) is zero.

For simplicity, we define

$$X \equiv \left. \frac{V_c^2}{V_d^2} \right|_{R_p}. \quad (4.6)$$

Therefore  $X = 2$  when the contribution of the disc to the circular speed curve at its peak is equal to the combined contributions of the dynamically hot components, namely the bulge and halo. Following Efstathiou et al. (1982), Yurin and Springel (2015), use  $Q_{\text{bar}} = V_{\text{max}} / (GM_d/R_d)^{1/2}$  where  $V_{\text{max}}$  is the maximum circular speed. If we assume that  $V_{\text{max}} \simeq V_c(R_p)$ , then  $Q_{\text{bar}}^2 \simeq 0.387X$  and the stability criterion from Efstathiou et al. (1982),  $Q_{\text{bar}} > 1.1$ , becomes  $X > 3.13$ .

#### 4.3.2 Vertical Structure of Stellar Discs

As discussed in Klypin et al. (2009) the vertical structure of a stellar disc plays a key role in determining the properties of any bar that forms. In general, the vertical structure is characterized by the vertical velocity dispersion  $\sigma_z$ , surface density  $\Sigma$ , and scale height. For a self-gravitating plane-symmetric isothermal disc these quantities are connected through the relation  $\sigma_z^2 = \sqrt{12}G\Sigma z_{\text{rms}}$  where  $z_{\text{rms}}$  is the root mean square distance of “stars” from the midplane. (Spitzer, 1942; Camm, 1950).

We can incorporate the effects of dark matter by modifying the Poisson equation

$$\begin{aligned} \frac{d^2\Phi}{dz^2} &= 4\pi G (\rho_d(z) + \rho_h(z)) \\ &= 4\pi G \rho_0 \left( e^{-\Phi/\sigma_z^2} + \rho_h/\rho_0 \right) \end{aligned} \quad (4.7)$$

where  $\rho_d$  and  $\rho_h$  are the densities of the disc and halo, respectively, and  $\rho_0$  is the density of the disc in the midplane. In the second line we assume, as is done in the pure self-gravitating case, that the disc stars are vertically isothermal with velocity

dispersion  $\sigma_z$ . We also assume that the halo density is constant in the region of the disc. We then solve Eq. 4.7 numerically. The result is well-described by the relation

$$\sigma_z^2 = \sqrt{12} G \Sigma z_{\text{rms}} (1 + \alpha \rho_h / \rho_0) \quad (4.8)$$

where the factor  $1 + \alpha = 1 + \sqrt{2\pi/3}$  provides a simple interpolation between the pure self-gravitating case and the case where disc particles are test particles in the (harmonic) potential of a constant density halo. As discussed in the next section Eq. 4.8 holds at the 10 per cent level for our equilibrium models. Departures from Eq. 4.8 might come from radial gradients and the rotation of the disc. (See, for example, Read (2014)).

Combining Eqs. 4.1, 4.6, 4.8 we find following relation:

$$\frac{Q^2}{X} = 3.103 \frac{\sigma_R^2}{\sigma_z^2} \frac{z_{\text{rms}}}{R_d} f \left( 1 + \frac{d \ln V_c}{d \ln R} \right). \quad (4.9)$$

This expression can be interpreted in several ways. First, if the ratios of  $\sigma_R$  to  $\sigma_z$  and  $z_{\text{rms}}$  to  $R_d$  are fixed, then there is a linear relation between  $Q^2$  and  $X$ . On the other hand, if one considers a family of models in which the only variation is in the vertical structure of the disc, then the scale height varies roughly linearly with the vertical velocity dispersion, apart from corrections due to the contribution of the halo to the vertical force.

### 4.3.3 Effect of Gravitational Softening

Numerical effects can significantly alter the development of bars in simulated galaxies. For example, in simulations of an isolated galaxy that is initially in equilibrium, the onset of bar formation is delayed when mass resolution is increased (Dubinski et al.,

2009) essentially because the bar instability is seeded by shot noise. The importance of mass resolution as well as force resolution and time stepping are also discussed in Klypin et al. (2009).

In this section, we focus on the effects of force softening. Equilibrium models, such as the ones used as initial conditions in isolated galaxy simulations, satisfy the collisionless Boltzmann and Poisson equations. When evolved with force softening, they will begin slightly out of equilibrium. This effect should be most noticeable when the softening length is comparable to or larger than the thickness of the disc. To gain some intuition as to this extent of this effect we solve the Poisson equation in one dimension. The potential for a mass distribution with vertical density profile of  $\rho(z)$  can be calculated by convolving  $\rho$  with the Green's function:

$$\Phi(z) = 4\pi G \int_{-\infty}^{\infty} \mathcal{G}(z' - z) \rho(z') dz' . \quad (4.10)$$

For Newtonian gravity,  $\mathcal{G} = |z|/2$ . For softened gravity, we replace  $\mathcal{G}$  with  $\mathcal{G}_s = \frac{1}{2} (z^2 + \epsilon^2)^{1/2}$  where  $\epsilon$  is the softening length. (The motivation for this expression is as follows: Begin with a system of Plummer-softened particles, that is, a system where point-like particles are replaced by particles whose spherical density profile is proportional to  $(r^2 + \epsilon^2)^{-5/2}$ . If the particles are confined to a plane, then the vertical density profile will be  $\rho(z) \propto (z^2 + \epsilon^2)^{-3/2}$ . The one-dimensional potential with this  $\rho(z)$  is indeed proportional to  $(z^2 + \epsilon^2)^{1/2}$ .) The integral Eq. 4.10 and the related integral for the vertical force,  $f(z)$ , can be evaluated numerically. As expected, the potential energy per unit area of the system,  $W \equiv \int dz \rho(z) z f(z)$  is smaller than that of the same system found assuming Newtonian gravity. Hence, a system that is set up to be in equilibrium under the assumption of Newtonian gravity, will be

too “warm” for a softened gravity simulation and will “puff up”. To an excellent approximation, we find that the virial ratio between the kinetic energy per unit area and  $W$  is given by  $2T/W \simeq (1 + (a\epsilon/z_{\text{rms}})^2)^b$  where  $a = 1.25$  and  $b = 0.25$ . Roughly speaking, simulations run with a softening length equal to  $z_{\text{rms}}$  will have a virial ratio of 1.25.

Softening may have other effects on the development of the bar. In principle, softening should suppress the Toomre instability on small scales. However, this instability develops on scales comparable to or larger than the Jeans length, which is typically much larger than the thickness of the disc and hence larger than the softening length for most simulations. On the other hand, softening may suppress buckling, a bending instability, which is strongest on small scales. As discussed below, buckling appears to be responsible for regulating the growth of bars.

#### 4.4 Models and Simulations

##### 4.4.1 Initial Conditions for Isolated Galaxy Simulations

We follow the evolution of isolated disc-halo systems using the N-body code GADGET-3 (Springel, 2005). The initial conditions for most of our isolated galaxy simulations are generated with GALACTICS (Kuijken and Dubinski, 1995; Widrow et al., 2008), which allows users to build multicomponent, axisymmetric equilibrium systems with prescribed structural and kinematic properties. Disc particles are sampled from a distribution function (DF) that is a semi-analytic function of the total energy  $E$ , the angular momentum about the disc symmetry axis  $L_z$ , and the vertical energy  $E_z = \Phi(R, 0) - \Phi(R, z) + \frac{1}{2}v_z^2$ , where  $\Phi$  is the gravitational potential and  $v_z$  is an orbit’s vertical velocity. By design, the disc DF yields a density law in cylindrical  $(R, \phi, z)$

coordinates given, to a good approximation, by  $\rho(R, z) = \Sigma(R) \text{sech}^2(z/z_d)$ . Here  $\Sigma(R)$  is exponential surface density profile (Eq. 4.4) and  $z_d$  is the scale height. Note that  $z_{\text{rms}} = \pi/\sqrt{12}z_d$  while the “half-mass” scale height used in Yurin and Springel (2015) is given by  $z_{1/2} \simeq 0.549z_d \simeq 0.605z_{\text{rms}}$ . The disc DF is also constructed to yield a radial velocity dispersion profile that is exponential in  $R$  with scale length  $2R_d$ . The halo DF is designed to yield a truncated NFW profile (Navarro et al., 1997) as described in Widrow et al. (2008).

While  $E_z$  used in the GALACTICS disc DF is conserved to a good approximation for nearly circular orbits it varies considerable for stars that make large excursions in  $R$  and  $z$ . Thus, the initial conditions for “thick” or “warm” discs will not represent true equilibrium solutions to the dynamical equations. To test whether non-conservation of vertical energy affects our results, we compare a thick disc model with GALACTICS initial conditions with a similar one where the initial conditions are generated with AGAMA (Vasiliev, 2018). In principle, this action-based code should yield initial conditions that are closer to a true equilibrium system than ones based on  $E_z$  especially for thick discs.

#### 4.4.2 Description of simulations

In this section, we describe a suite of simulations where  $Q$  and  $X$  are fixed and where the velocity dispersion and scale length ratios are allowed to vary. Our aim is to test the hypothesis that scale height plays a key role in the development of bars. The parameters for our simulations are summarized in Table 4.1. Our suite of isolated galaxy simulations form a sequence A, B, C in increasing thickness. The models have the same rotation curve decomposition, which is shown in the top panel of Fig. 4.1.

By design, the contribution to the rotation curve from the disc is slightly below that of the halo at  $R_p$ . Therefore our models have  $X$  slightly greater than 2 and should be susceptible to global instabilities.

The fiducial simulations are run with a softening length of 184, pc, which is about two thirds of the scale height of our thinnest model (A.I). The simulations A.II and B.II use a softening length of 736 pc, which is close to the value assumed in Yurin and Springel (2015). The simulation C.I.Ag is similar to C.I (large scale height) but run with AGAMA initial conditions. A comparison of its rotation curve decomposition with that for model C.I is shown in the top panel of Fig. 4.1. The contributions from the disks in the two models are nearly the same and the contributions from the halos differ significantly only beyond  $\sim 10$  kpc. The simulations A.III and B.III use a scheme to isotropize vertical motions and effectively shut off buckling and are discussed in §4.5.4.

In addition to these isolated galaxy simulations we run two cosmological simulations using the disc insertion scheme described in Bauer et al. (2018). The initial conditions for these models, labeled D.I and E.II, are identical except for the vertical scale height and softening length, which are larger in E.II. Thus, these models are cosmological analogs to A.I and B.II. The rotation curves for these models are shown in the bottom panel of Fig. 4.1. The models themselves are discussed in Section §4.6.

#### 4.4.3 Comparison with Previous Work

While the parameters  $Q$  and  $X$  allow one to predict the rapidity and vigour with which instabilities develop in disc galaxies that are actually imperfect predictors of the strength and length of bars at late times. The point is illustrated in Widrow

et al. (2008) where results for a suite of 25 simulations that explore the  $Q - X$  plane are presented. By design, the initial conditions for the models satisfy observational constraints for the Milky Way such as the rotation curve, the local vertical force, and the velocity dispersion toward the bulge. (See Hartmann et al. (2014) for a further analysis of these simulations.) As expected, the onset of the bar instability is delayed in models with large initial values for  $Q$  and/or  $X$ . However, the dependence on these parameters of the bar strength and length is more complicated. In Fig.4.4 we show the bar strength parameter  $A_2$  and length of the bar across these models. Evidently, the models that form the strongest and longest bars have intermediate values of  $Q$  and  $X$ . The implication is that models where the instabilities grow too quickly lead to weaker and somewhat shorter bars. Bar formation appears to be a self-regulating process.

Table 4.1 gives the relevant parameters for the eight disc-halo models from Yurin and Springel (2015) as well as the disc-bulge-halo model for M31 from Gauthier et al. (2006). In the Yurin and Springel (2015) simulations discs are inserted into dark matter haloes from the cosmological Aquarius simulation. In this respect, they are similar to the disc-insertion simulations described in Section §4.6. The initial discs in these models all have a scale height to scale length ratio of 0.2 and a radial to vertical velocity dispersion ratio of 1. As discussed above, these choices mean that their discs were chosen from a one-parameter family of models within the  $Q - X$  parameter space.



## 4.5 Isolated Galaxy Simulations

### 4.5.1 Morphology of Bar Forming Galaxies

Face on surface density maps for models A.I, A.II, B.I, B.II, C.I, and C.I.Ag are shown in Fig. 4.5. All discs form bars by the end of the simulation ( $t = 10$  Gyr). However, bar formation appears to be delayed in models B.I and C.I relative to that in model A.I while the final bar in A.I is shorter than those in B.I and C.I. Other  $m = 2$  features are also evident. These include two-armed spiral structure, most clearly seen in A.I and B.III and elliptical rings, as, for example, in C.I.

Evidently, the dominant mode for in-plane perturbations is  $m = 2$ . Nevertheless, there are strong  $m = 3$  structures in the 1.5 Gyr snapshot of the A.I and A.II simulations and hints of a weak  $m = 3$  structure in the same snapshot of B.II.

A larger softening length seems to lead to stronger bars at intermediate times. We see this in the comparison of A.I and A.II or B.I and B.II in the 3.0 Gyr and 4.5 Gyr snapshots.

### 4.5.2 Bar Strength Parameter $A_2$

It is convenient to think of the azimuthal distribution of particles in a given radial bin as a Fourier series. We define the coefficient of the Fourier component with  $m$ -fold azimuthal symmetry to be

$$c_m = \frac{1}{M_S} \sum_{j \in S} \mu_j e^{im\phi} \quad (4.11)$$

where  $\mu_i$  is the mass of the  $i$ -th particle and  $S$  is a circularly symmetric region of the disc. The normalization is chosen so that a distribution of particles along a line through the origin will have  $|c_m| = 1$  for all  $m$  even. Moreover, for a uniform

distribution of particles,  $c_0 = 1$  and  $c_m = 0$  for all  $m > 0$ . The amplitude and phase for the  $m$ -th Fourier coefficient are given by  $A_m \equiv |c_m|$  and  $\phi_m = \arg c_m$ , respectively. Note that both of these quantities depend on the region  $S$

Fig. 4.6 shows a plot of the mean  $A_2$  inside the radius  $R_p$  as a function of time for the fiducial simulations, the two simulations with high softening, and the thick disc simulation with initial conditions from AGAMA. Consider first the fiducial (low-softening) simulations. Initially,  $A_2$  grows roughly exponentially with a growth rate that decreases with increasing thickness. In simulations A.I and B.I, the end of exponential growth is followed by a decrease in  $A_2$  after which  $A_2$  again increases, now, approximately linearly with time. In the thick disc case (C.I) exponential growth transitions directly to linear growth. The trend is for exponential growth to end at later times as one goes to thicker discs. It is worth noting that the value of  $A_2$  at 10 Gyr is similar in the three low-softening simulations.

In the thin disc case, an increase in softening appears to delay the onset of exponential growth as well as the time at which exponential growth ends. Furthermore, the drop in  $A_2$  is less severe. Though the value of  $A_2$  at the end of the simulation is approximately the same in the low and high softening cases, the bar strength, as measured by  $A_2$  is larger in the high-softening case at intermediate times between 4 and 8 Gyr. For the intermediate thickness case (B.I and B.II) softening has little effect on the initial growth rate of  $A_2$ . But as in the thin disc case, softening allows exponential growth to continue to later times and the final bar is about twenty per cent stronger as compared with the low-softening case. Once again we see that the effect of high softening is to produce stronger bars at intermediate times.

The evolution of  $A_2$  for the thick disc runs with GALACTICS and AGAMA initial

conditions are fairly similar. In particular, the initial growth rate is almost identical as are the final values.

Fig. 4.6 encapsulates bar strength into a single number, the mean  $m = 2$  Fourier amplitude inside 2.2 disc scale lengths, or about 5.5 kpc. A more complete picture of bar strength is presented in Fig. 4.7 where we plot  $A_2$  as a function of  $R$  and  $t$ . The figure is constructed by calculating  $c_2$  (Eq. 4.11) for cylindrical rings of radius 200 pc. Also shown is the corotation radius, which is determined from the pattern speed  $\Omega_p$  and rotation curve. The former is given by a numerical estimate of  $d\phi_2/dt$ ; corotation is found by determining the radius at which  $\Omega_p = V_c/R$ . Thus, since our galaxy models have roughly flat rotation curves beyond 5 kpc, the corotation essentially gives the inverse pattern speed or pattern period.

From Fig. 4.6 we see that the corotation radius tends to grow with time and provides an envelope for the bar and other  $m = 2$  structures such as two-armed spirals and elliptical rings. The bar pattern speed is therefore decreasing with time, presumably due to dynamical friction between the bar and both the disc and dark halo (Debattista and Sellwood, 1998, 2000). It is worth noting that the corotation radius increases more rapidly in simulations with high softening. The naive interpretation is that softening somehow increases the frictional coupling between the bar and disc or halo particles. A more likely explanation is that with a high softening length comes stronger bars. Since the acceleration on the bar due to dynamical friction scales as the mass of the bar, stronger bars should spin down more rapidly.

As in Fig. 4.6 we see that bar formation is delayed in models with thicker discs. Bar formation is well underway by 2 Gyr in A.I but doesn't really take hold until 4 Gyr in C.I. Moreover, the first hints of  $m = 2$  power in C.I arise further out at radii

closer to 5 kpc.

The dip in bar strength is clearly seen between 2.5 – 3 Gyr in A.I and between 3.5 – 4 Gyr in B.I. As discussed below, we attribute this dip to buckling.

### 4.5.3 Vertical Structure and Velocity Dispersion

Figs. 4.8 and 4.9 show the  $z_{\text{rms}}$  and velocity dispersion profiles for a sequence of snapshots in various models. The first of these plots focuses on the evolution of  $z_{\text{rms}}$  during the initial 500 Myr of the simulation. The top panels show the  $z_{\text{rms}}$  profiles for simulations A.I and A.II and illustrate the effect softening has on the evolution from “equilibrium” initial conditions. As discussed in Section 2 a system that is initialized to be in equilibrium under the assumption of Newtonian gravity will be out of equilibrium if evolved with softened gravity. In particular, the mean potential energy will be systematically low and the system will puff up. For our thin disc model,  $z_{\text{rms}} \simeq 230$  pc. In the high softening case,  $\epsilon = 736$  pc  $\simeq 2.2z_{\text{rms}}$ , we estimate the virial ratio for the vertical structure to be  $2T/W \simeq 1.7$ . Of course, the excess kinetic energy will redistribute itself into both kinetic and potential energy. The upshot is that the system quickly settles into a new state with a thickness somewhat larger than the initial one as seen in the right hand panel.

The bottom panels in Fig. 4.8 provide a comparison of  $z_{\text{rms}}$  profiles for the thick disc simulations with GALACTICS and AGAMA initial conditions. We first note that  $z_{\text{rms}}$  is approximately constant in the C.I but varies by about 200 pc in C.I.Ag. This difference is simply a reflection in how the initial conditions are set up. In both cases, the scale height depends implicitly on the functional form of the DFs, which are written in terms of either  $E$ ,  $E_z$ , and  $L_z$  or the actions. The GALACTICS case does

exhibit transient wavelike perturbations with a peak to trough amplitude of 100 pc at radii  $R > 4$  kpc. A plausible explanation for these oscillations is that they are due to the fact that  $E_z$  is not a true constant of motion. In any case, the system quickly settles to a new equilibrium state not too different from the initial one.

Fig. 4.9 shows profiles for  $z_{\text{rms}}$  and the diagonal components of the velocity dispersion tensor,  $\sigma_z$ ,  $\sigma_R$ , and  $\sigma_\phi$ . The effect of bar formation is readily apparent in the  $z_{\text{rms}}$  and  $\sigma_z$  profiles. In simulation A.I, for example, bar formation, which begins around  $t \simeq 1.5$  Gyr is accompanied by thickening and vertical heating. By the end of the simulation,  $z_{\text{rms}}$  increases linearly with  $R$  from a central value of about 400 pc to 1.5 kpc at a radius of about 6 – 7 kpc and then decreases beyond this radius. The evolution is similar in simulations B.I and C.I. Interestingly enough, the central and peak values are very similar in all three cases even though the initial thick of the discs are very different. Indeed, the central value for  $z_{\text{rms}}$  actually decreases with time in our thick disc simulation.

Vertical heating of the disc in the central regions also seems to be connected with bar formation, at least in the thin and intermediate thickness cases. In A.I, for example, the central velocity dispersion appears to increase rapidly starting around 3 Gyr and reaching a final value of  $\sim 100 \text{ km s}^{-1}$ , which is roughly a factor of two larger than the initial value. As with  $z_{\text{rms}}$ , the value of the central vertical velocity dispersion is nearly identical in all models. Evidently, the final vertical structure of the barred disc is insensitive to initial conditions.

All models show significant in-plane disc heating across the disc and throughout the simulation. While the initial radial velocity dispersion profile is exponential in  $R$  the final profile is almost flat within the central 5 kpc. Thus, the greatest increase in

radial velocity dispersion is at about this radius, which corresponds to the end of the bar. On the other hand, the greatest increase in  $\sigma_\phi$  occurs at larger radii, closer to 10 kpc.

#### 4.5.4 Simulations Where Buckling is Suppressed

Buckling is a well-known phenomena often seen in simulations of bar-forming galaxies where the bar bends in and out of the disc plane. Eventually, these coherent oscillations are converted to random vertical motions (Binney and Tremaine, 2008). Buckling typically leads to shorter and weaker bars (Martinez-Valpuesta and Shlosman, 2004)

To isolate the effects of buckling we implement a simple scheme that prevents the instability from taking hold. Essentially, at each timestep, we reverse the vertical components of the position, velocity, and acceleration for a fraction  $p$  of disc particles. In practice, we choose  $p = 0.25$  though the results are insensitive to the exact value.

Fig. 4.10 shows the effect suppressing buckling has on the disc evolution. In the thin disc case, the bar instability develops a bit faster when buckling is suppressed. More importantly, the drop in  $A_2$  seen in simulation A.I is not as strong, thus confirming the notion that buckling regulates the strength of bars. Buckling has a similar effect on our intermediate thickness runs. Furthermore, the effect of suppressing buckling is similar, in some respects, to the effect of increasing softening as can be seen by noting similarities between A.II and B.III. Finally, we note that buckling doesn't appear to occur in our thick disc simulations.

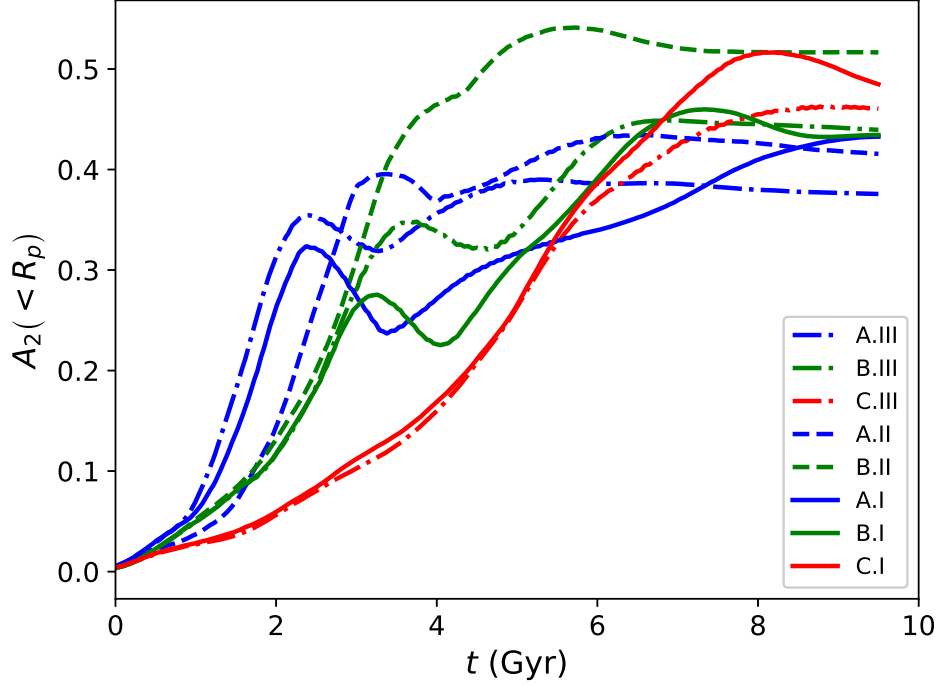


Figure 4.10: Mean bar strength parameter inside the cylindrical radius  $R_p$ ,  $A_2(< R_p)$ , as a function of time. The figure is essentially the same as Fig. 4.6 though this time we include simulations A.III, B.III, and C.III where buckling is suppressed.

#### 4.6 Cosmological Simulations

Disc galaxies simulated from axisymmetric, equilibrium initial conditions, as was done in the previous section, form bars at rates and with strengths that depend on their intrinsic scale height of the disc and on the force resolution of the simulation. In this section, we investigate the extent to which these results hold in a cosmological environment. In particular we follow the evolution of a thin disc with moderate softening and a thick disc with high softening that are embedded in identical cosmological haloes.

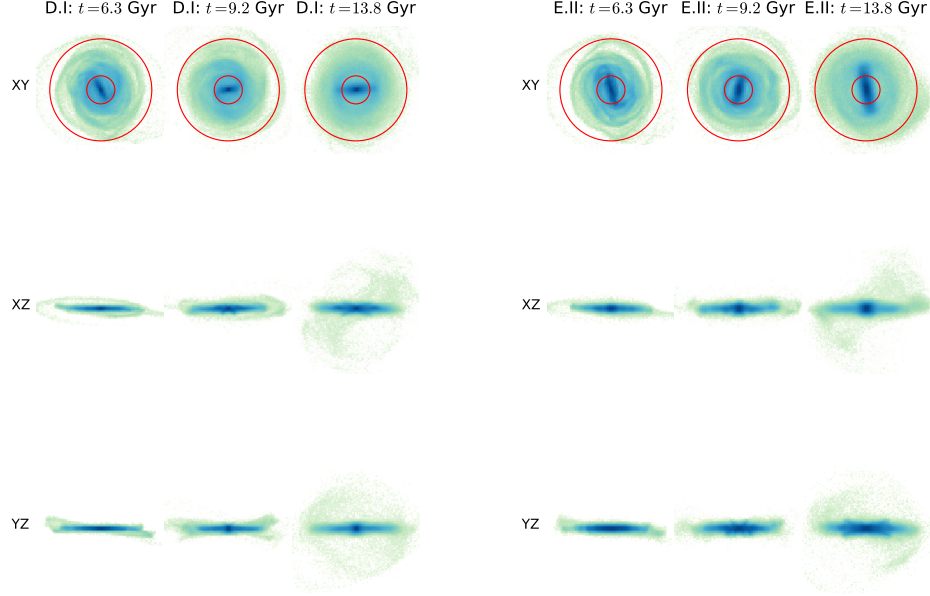


Figure 4.11: Projections for the D.I (left three columns) and E.II (right three columns). The three columns for each simulation correspond, from left to right, to 2.2 Gyr, 5.9 Gyr, and 13.7 Gyr after the Big Bang. The overlaid red circles have radii  $R_p$  and  $20 h^{-1} \text{ kpc}$ .

#### 4.6.1 Simulation Setup; Inserting Discs into Cosmological Haloes

We model a stellar disc in a cosmological halo using the disc insertion scheme described in Bauer et al. (2018). This scheme, which builds on the methods developed by Berentzen and Shlosman (2006), DeBuhr et al. (2012), and Yurin and Springel (2015) uses an iterative procedure to initialize the disc. The first step is to run a pure dark matter simulation and identify a suitable halo. The system is then rerun from redshift  $z_g$  to  $z_l$ , this time with a disc potential that grows slowly in mass and



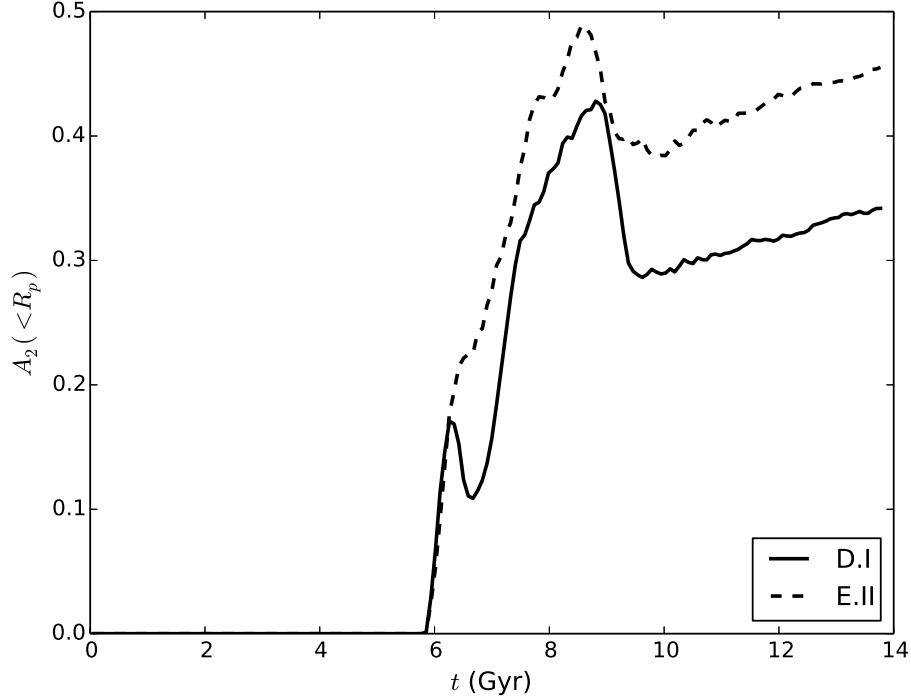


Figure 4.12:  $A_2(< R_p)$  as a function of the age of the Universe for simulations D.I (solid curve) and E.II (dashed curve).

radius. Doing so allows the halo particles to respond to the gravitational field of the would-be disc. At  $z_l$ , the rigid disc is replaced by an N-body system and the “live” disc-halo system is evolved to the present epoch.

For our pure dark matter simulation, we implement the zoom-in technique of Katz et al. (1994) and Navarro et al. (1994), broadly following the recommendations of Oñorbe et al. (2014), which allows us to achieve very high spatial and mass resolution for a single halo while still accounting for the effects of large-scale tidal fields. We choose cosmological parameters based on the results from Planck 2013 (Planck Collaboration et al., 2014) with  $H_0 = 67.9 \text{ km s}^{-1} \text{ kpc}^{-1}$ ,  $\Omega_b = 0.0481$ ,  $\Omega_0 = 0.306$ ,

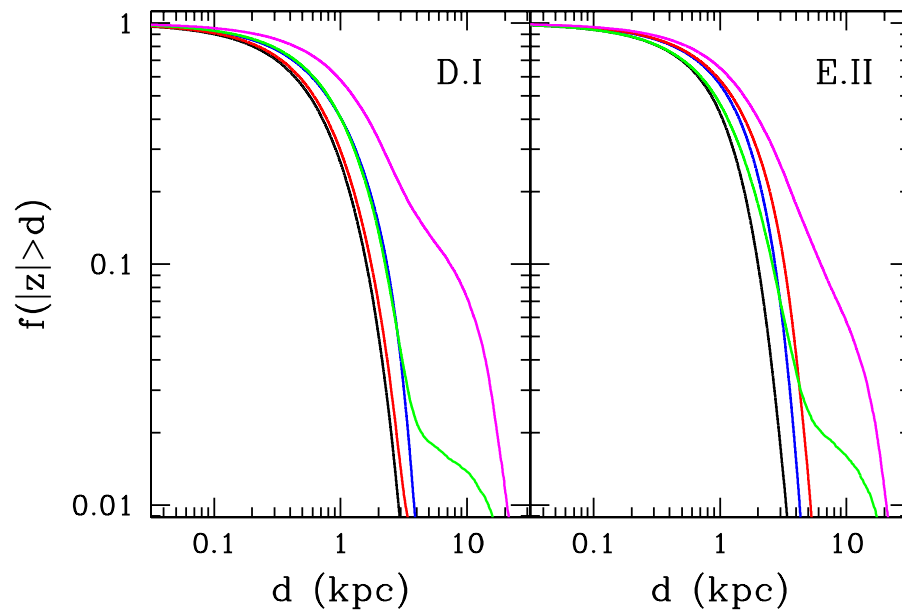


Figure 4.13: Fraction of particles with distance from the midplane greater than some distance  $d$  as a function of  $d$ . The different colours correspond to different bins in cylindrical radius  $R$ :  $0 < R < 5$  kpc — black;  $5$  kpc  $< R < 10$  kpc — blue;  $10$  kpc  $< R < 15$  kpc — red;  $15$  kpc  $< R < 20$  kpc — green;  $20$  kpc  $< R$  kpc — magenta.

$\Omega_\Lambda = 0.694$ ,  $\sigma_8 = 0.827$ , and  $n_s = 0.962$ . N-body initial conditions for the dark matter particles are generated with the MUSIC code (Hahn and Abel, 2013). We select a suitably-sized halo for a Milky Way-like galaxy, namely one with a  $z = 0$  mass of  $1.23 \times 10^6 h^{-1} M_\odot$  that comprises  $10^6$ .

During its growth phase from  $z_g = 3$  to  $z_l = 1$ , the disc is treated as a rigid body whose orientation and center-of-mass position evolve according to the standard equations of rigid body dynamics. At  $z_l$ , we swap a live disc for the rigid one using the GALACTICS code (Kuijken and Gilmore, 1989; Widrow et al., 2008), which generates a three-integral DF disc in the best axisymmetric approximation to the halo Bauer et al. (2018).

We run two simulations, D.I, which assumes a thin disc with a softening length of 184 pc and E.II, which assumes a thick disc with a softening length of 736 pc. The softening length chosen for D.I is in accord with the criteria outlined in Power et al. (2003). The simulations D.I and E.II roughly correspond to A.I and B.II, respectively. As well, E.II is similar to the discs considered by DeBuhr et al. (2012), Yurin and Springel (2015) and Bauer et al. (2018), whereas D.I is more consistent with typical discs considered in isolated galaxy suites like Widrow et al. (2008).

#### 4.6.2 Results

Results from our two cosmological simulations are displayed in Figs. 4.11 and 4.12. The former shows projections of the mass density at three epochs while the latter gives  $A_2(< R_p)$  as a function of time. Evidently, the discs in both cases roughly follow the same evolutionary sequence that was seen in the isolated galaxy simulations: rapid growth of the bar strength followed by a period where the bar strength decreases,

presumably due to buckling, and finally steady strengthening of the bar. The three epochs chosen in Fig. 4.11 correspond to the initial growth phase of the bar ( $a = 0.6$ ,  $t = 6.3$  Gyr), an epoch after buckling ( $a = 0.7$ ,  $t = 9.2$  Gyr), and the present epoch at  $t = 13.8$  Gyr. Visually, the bar appears to be stronger and longer in the E.II run than D.I one at each of these epochs but perhaps most notably in the final one. Indeed, the disc in E.II looks very similar to those seen in the simulations of DeBuhr et al. (2012), Yurin and Springel (2015), and Bauer et al. (2018). The fact that the bar in D.I is weaker than the one in E.II is consistent with the results from our isolated galaxy simulations that thicker discs produce stronger bars (See Fig. 4.5.

The most significant difference between bar formation in the cosmological setting and bar formation in isolated galaxies concerns the initial growth of the bar. For isolated galaxies, Fig. 4.6 clearly shows that the onset of bar formation is delayed for thicker discs. Conversely, in the cosmological case,  $A_2$  rapidly grows to a value of  $\sim 0.17$  within the first few hundred Myr after the disc “goes live” regardless of the disc thickness. At this point, the bar in the thin disc model decreases in strength with  $A_2$  dropping to  $\sim 0.11$  before resuming its growth. By contrast, the bar in the thick disc model continues to grow monotonically. As in the isolated galaxy simulations, self-regulating processes such as buckling are more efficient in the thin disc case and so  $A_2$  in simulation D.I lags behind that of E.II. We note that in both cases,  $A_2$  drops significantly at around  $t = 7.5$  Gyr and grows steadily thereafter.

Our interpretation of these results is as follows: In isolation, where discs start from axisymmetric initial conditions, the only source of the  $m = 2$  perturbations that drive bar formation is shot noise from the N-body distribution. Evidently, making a disc thicker slows the growth of these perturbations. On the other hand,  $m = 2$

perturbations abound in the cosmological environment where halos are clumpy and triaxial. The initial growth of the bar may, in fact, be relatively insensitive to the thickness of the disc, once discs are placed in a cosmological setting. On the other hand, disc thickness does effect the resilience of the bar to self-regulating processes, such that buckling and therefore thick discs tend to have stronger bars.

Finally, we note that in both D.I and E.II, a significant number of particles are found at high galactic latitudes. These particles represent stars “kicked-up” from the disc presumably by the large-scale tidal fields of the halo and interactions between the disc and halo substructure. Kicked-up stars have been seen in cosmological simulations by Purcell et al. (2010), McCarthy et al. (2012) and Tissera et al. (2013). Their existence was inferred in a combined analysis of kinematic and photometric data for the Andromeda galaxy (Dorman et al., 2013). Furthermore, the idea of kicked-up stars has been invoked by (Price-Whelan et al., 2015) to explain the Triangulum-Andromeda stellar clouds (Rocha-Pinto et al., 2003; Martin et al., 2014) and by (Sheffield et al., 2018) to explain the Monoceros Ring (Yanny et al., 2000; Newberg et al., 2002) and associated A13 stellar overdensity (Sharma et al., 2010).

In Fig. 4.13 we show the fraction of stars with  $|z| > d$  for different regions of the discs in our two cosmological simulations. The results are strikingly similar for the two simulations as is already evident from a visual inspection of Fig. 4.11. The implication is that the processes by which stellar orbits are perturbed out of the disc plane are relatively insensitive to the vertical structure of the disc. We see that very few of the stars with cylindrical radius  $R < 15$  kpc and only  $1 - 2\%$  of the stars between 15 and 20 kpc are kicked-up to distances greater than 3 kpc though some stars from the 15 – 20 kpc region do end up with  $|z| > 10$  kpc. On the other hand,

20 % of the stars from the region beyond 20 kpc end up with  $|z| > 3$  kpc from the midplane and 10 10 kpc. Of course, the actual number of stars is certainly larger since a fraction of the kicked-up stars will be passing through the disc with large vertical velocities.

#### 4.7 Conclusions

The seminal work of Ostriker and Peebles (1973) introduced the notion that disc dynamics provides a powerful constraint on the structure of discs and the halos in which they reside. In short, discs that are dynamically cold and that account for a substantial fraction of the gravitational force that keeps their stars on nearly circular orbits are unstable to the formation of strong bars and spiral structure. The existence of galaxies with weak bars or no bars at all tells us that at least some discs are relatively low in mass (i.e., submaximal) and/or dynamically warm.

The theoretical analysis presented in Section 2 showed with a few simple assumptions (e.g., exponential surface density profile) one can derive a relation among the structural parameters of a disc in approximate equilibrium and thus a constraint on initial conditions that one might choose for simulations. For example, if one fixes  $h_d/R_d$  and  $\sigma_R/\sigma_z$ , as was done in Yurin and Springel (2015), then there is an approximately one-to-one relationship between  $Q$  and  $X$ . Likewise, fixing  $Q$  and  $X$  implies a relationship between  $h_d/R_d$  and  $\sigma_R/\sigma_z$ . These results have important implications for applying disc dynamics as a constraint on models of galaxy formation. In particular, inconsistencies between bar demographics in a galaxy formation model and in observational surveys may reflect differences in the scale height and vertical velocity dispersion of model and real galaxies.

One lesson from our work and the work of others is that the relation between structural parameters of galaxies and bar strength and length is often rather complicated. This observation is no doubt due, at least in part, to the self-regulating nature of bar formation. When bars develop rapidly, they tend to buckle, which leads to weaker and shorter bars (Martinez-Valpuesta and Shlosman, 2004). Thick discs appear to be more resilient to buckling, which may explain why bars in these models often end up stronger and longer than bars in thin-disc models (Klypin et al., 2009). For similar reasons, gravitational softening can affect the development and ultimate strength of bars.

In simulations of isolated galaxies from “pristine” equilibrium initial conditions, bar formation is seeded by the shot noise of the N-body distribution. On the other hand, bars in a cosmological environment are subjected to large perturbations including the  $m = 2$  ones that drive bar formation. Thus, the fact that bar formation is delayed in thick disc models of isolated galaxies may be purely academic — bar formation in the cosmological environment will be initiated by a variety of stochastic effects regardless of the thickness of the disc. On the other hand, the resilience of thick disks to buckling *is* relevant in the cosmological setting and may explain why thick disks tend to form strong bars. The upshot is that a proper understanding the distribution of bars in cosmological models must go hand-in-hand with a proper understanding of the vertical structure of discs.

Clearly, a more exhaustive exploration of the model parameter space is in order. One might, for example, include galaxy scaling relations to further constrain the space of models. In addition, it would be of interest to insert different discs (and for that matter, nearly identical ones) into different halos in order to explore the random

nature of disc-halo interactions. Ultimately, improvements in observations together with a more complete survey of models via simulations should allow us to fully exploit bars in discs as a means of testing and constraining theories of structure formation.

### **Acknowledgements**

LMW and JB are supported by a Discovery Grant with the Natural Sciences and Engineering Research Council of Canada. JSB acknowledges the assistance of Matthew Chequers and Keir Darling in understanding the AGAMA program interface.



## Bibliography

- Athanassoula, E. and Sellwood, J. A. (1986). Bi-symmetric instabilities of the Kuz'min/Toomre disc. *MNRAS*, 221:213–232.
- Bauer, J. S., Widrow, L. M., and Erkal, D. (2018). Disc-Halo Interactions in  $\Lambda$ CDM. *ArXiv e-prints*.
- Berentzen, I. and Shlosman, I. (2006). Growing Live Disks within Cosmologically Assembling Asymmetric Halos: Washing Out the Halo Prolateness. *ApJ*, 648:807–819.
- Binney, J., Jiang, I.-G., and Dutta, S. (1998). The Persistence of WARPS in Spiral Galaxies with Massive Haloes. *MNRAS*, 297:1237–1244.
- Binney, J. and Tremaine, S. (2008). *Galactic Dynamics: Second Edition*. Princeton University Press.
- Blumenthal, G. R., Faber, S. M., Flores, R., and Primack, J. R. (1986). Contraction of dark matter galactic halos due to baryonic infall. *ApJ*, 301:27–34.
- Camm, G. L. (1950). Self-gravitating star systems. *MNRAS*, 110:305.

- Christodoulou, D. M., Shlosman, I., and Tohline, J. E. (1995). A new criterion for bar-forming instability in rapidly rotating gaseous and stellar systems. 2: Nonaxisymmetric form. *ApJ*, 443:563–569.
- Combes, F. and Sanders, R. H. (1981). Formation and properties of persisting stellar bars. *A&A*, 96:164–173.
- Debattista, V. P. and Sellwood, J. A. (1998). Dynamical Friction and the Distribution of Dark Matter in Barred Galaxies. *ApJ*, 493:L5–L8.
- Debattista, V. P. and Sellwood, J. A. (2000). Constraints from Dynamical Friction on the Dark Matter Content of Barred Galaxies. *ApJ*, 543:704–721.
- DeBuhr, J., Ma, C.-P., and White, S. D. M. (2012). Stellar discs in Aquarius dark matter haloes. *MNRAS*, 426:983–999.
- Dorman, C. E., Widrow, L. M., Guhathakurta, P., Seth, A. C., Foreman-Mackey, D., Bell, E. F., Dalcanton, J. J., Gilbert, K. M., Skillman, E. D., and Williams, B. F. (2013). A New Approach to Detailed Structural Decomposition from the SPLASH and PHAT Surveys: Kicked-up Disk Stars in the Andromeda Galaxy? *ApJ*, 779:103.
- Dubinski, J. (1994). The effect of dissipation on the shapes of dark halos. *ApJ*, 431:617–624.
- Dubinski, J., Berentzen, I., and Shlosman, I. (2009). Anatomy of the Bar Instability in Cuspy Dark Matter Halos. *ApJ*, 697:293–310.
- Dubinski, J. and Chakrabarty, D. (2009). Warps and Bars from the External Tidal Torques of Tumbling Dark Halos. *ApJ*, 703:2068–2081.

- Dubinski, J. and Kuijken, K. (1995a). The settling of warped disks in oblate dark halos. *ApJ*, 442:492–503.
- Dubinski, J. and Kuijken, K. (1995b). The settling of warped disks in oblate dark halos. *ApJ*, 442:492–503.
- Efstathiou, G., Lake, G., and Negroponte, J. (1982). The stability and masses of disc galaxies. *MNRAS*, 199:1069–1088.
- Gauthier, J.-R., Dubinski, J., and Widrow, L. M. (2006). Substructure around M31: Evolution and Effects. *ApJ*, 653:1180–1193.
- Goldreich, P. and Tremaine, S. (1978). The excitation and evolution of density waves. *ApJ*, 222:850–858.
- Goldreich, P. and Tremaine, S. (1979). The excitation of density waves at the Lindblad and corotation resonances by an external potential. *ApJ*, 233:857–871.
- Hahn, O. and Abel, T. (2013). MUSIC: MUlti-Scale Initial Conditions. Astrophysics Source Code Library.
- Hartmann, M., Debattista, V. P., Cole, D. R., Valluri, M., Widrow, L. M., and Shen, J. (2014). The effect of bars on the  $M\text{-}\sigma_e$  relation: offset, scatter and residuals correlations. *MNRAS*, 441:1243–1259.
- Katz, N., Quinn, T., Bertschinger, E., and Gelb, J. M. (1994). Formation of Quasars at High Redshift. *MNRAS*, 270:L71.

- Kazantzidis, S., Bullock, J. S., Zentner, A. R., Kravtsov, A. V., and Moustakas, L. A. (2008). Cold Dark Matter Substructure and Galactic Disks. I. Morphological Signatures of Hierarchical Satellite Accretion. *ApJ*, 688:254–276.
- Klypin, A., Valenzuela, O., Colín, P., and Quinn, T. (2009). Dynamics of barred galaxies: effects of disc height. *MNRAS*, 398:1027–1040.
- Kuijken, K. and Dubinski, J. (1995). Nearly Self-Consistent Disc / Bulge / Halo Models for Galaxies. *MNRAS*, 277:1341.
- Kuijken, K. and Gilmore, G. (1989). The mass distribution in the galactic disc. I - A technique to determine the integral surface mass density of the disc near the sun. *MNRAS*, 239:571–603.
- Martin, N. F., Ibata, R. A., Rich, R. M., Collins, M. L. M., Fardal, M. A., Irwin, M. J., Lewis, G. F., McConnachie, A. W., Babul, A., Bate, N. F., Chapman, S. C., Conn, A. R., Crnojević, D., Ferguson, A. M. N., Mackey, A. D., Navarro, J. F., Peñarrubia, J., Tanvir, N. T., and Valls-Gabaud, D. (2014). The PAndAS Field of Streams: Stellar Structures in the Milky Way Halo toward Andromeda and Triangulum. *ApJ*, 787:19.
- Martinez-Valpuesta, I. and Shlosman, I. (2004). Why Buckling Stellar Bars Weaken in Disk Galaxies. *ApJ*, 613:L29–L32.
- Masters, K. L., Mosleh, M., Romer, A. K., Nichol, R. C., Bamford, S. P., Schawinski, K., Lintott, C. J., Andreescu, D., Campbell, H. C., Crowcroft, B., Doyle, I., Edmondson, E. M., Murray, P., Raddick, M. J., Slosar, A., Szalay, A. S., and Vandenberg, J. (2010). Galaxy Zoo: passive red spirals. *MNRAS*, 405:783–799.

- McCarthy, I. G., Font, A. S., Crain, R. A., Deason, A. J., Schaye, J., and Theuns, T. (2012). Global structure and kinematics of stellar haloes in cosmological hydrodynamic simulations. *MNRAS*, 420:2245–2262.
- Navarro, J. F., Frenk, C. S., and White, S. D. M. (1994). Accretion of Satellite Galaxies and the Density of the Universe. *MNRAS*, 267:L1.
- Navarro, J. F., Frenk, C. S., and White, S. D. M. (1997). A Universal Density Profile from Hierarchical Clustering. *ApJ*, 490:493–508.
- Newberg, H. J., Yanny, B., Rockosi, C., Grebel, E. K., Rix, H.-W., Brinkmann, J., Csabai, I., Hennessy, G., Hindsley, R. B., Ibata, R., Ivezić, Z., Lamb, D., Nash, E. T., Odenkirchen, M., Rave, H. A., Schneider, D. P., Smith, J. A., Stolte, A., and York, D. G. (2002). The Ghost of Sagittarius and Lumps in the Halo of the Milky Way. *ApJ*, 569:245–274.
- Oñorbe, J., Garrison-Kimmel, S., Maller, A. H., Bullock, J. S., Rocha, M., and Hahn, O. (2014). How to zoom: bias, contamination and Lagrange volumes in multimass cosmological simulations. *MNRAS*, 437:1894–1908.
- Ostriker, J. P. and Peebles, P. J. E. (1973). A Numerical Study of the Stability of Flattened Galaxies: or, can Cold Galaxies Survive? *ApJ*, 186:467–480.
- Planck Collaboration, Ade, P. A. R., Aghanim, N., Armitage-Caplan, C., Arnaud, M., Ashdown, M., Atrio-Barandela, F., Aumont, J., Baccigalupi, C., Banday, A. J., and et al. (2014). Planck 2013 results. XVI. Cosmological parameters. *A&A*, 571:A16.

- Power, C., Navarro, J. F., Jenkins, A., Frenk, C. S., White, S. D. M., Springel, V., Stadel, J., and Quinn, T. (2003). The inner structure of  $\Lambda$ CDM haloes - I. A numerical convergence study. *MNRAS*, 338:14–34.
- Price-Whelan, A. M., Johnston, K. V., Sheffield, A. A., Laporte, C. F. P., and Sesar, B. (2015). A reinterpretation of the Triangulum-Andromeda stellar clouds: a population of halo stars kicked out of the Galactic disc. *MNRAS*, 452:676–685.
- Purcell, C. W., Bullock, J. S., and Kazantzidis, S. (2010). Heated disc stars in the stellar halo. *MNRAS*, 404:1711–1718.
- Purcell, C. W., Bullock, J. S., Tollerud, E. J., Rocha, M., and Chakrabarti, S. (2011). The Sagittarius impact as an architect of spirality and outer rings in the Milky Way. *Nature*, 477:301–303.
- Read, J. I. (2014). The local dark matter density. *Journal of Physics G Nuclear Physics*, 41(6):063101.
- Rocha-Pinto, H. J., Majewski, S. R., Skrutskie, M. F., and Crane, J. D. (2003). Tracing the Galactic Anticenter Stellar Stream with 2MASS M Giants. *ApJ*, 594:L115–L118.
- Ryden, B. S. and Gunn, J. E. (1987). Galaxy formation by gravitational collapse. *ApJ*, 318:15–31.
- Schaye, J., Crain, R. A., Bower, R. G., Furlong, M., Schaller, M., Theuns, T., Dalla Vecchia, C., Frenk, C. S., McCarthy, I. G., Helly, J. C., Jenkins, A., Rosas-Guevara, Y. M., White, S. D. M., Baes, M., Booth, C. M., Camps, P., Navarro, J. F., Qu, Y., Rahmati, A., Sawala, T., Thomas, P. A., and Trayford, J. (2015). The EAGLE

- project: simulating the evolution and assembly of galaxies and their environments. *MNRAS*, 446:521–554.
- Sellwood, J. A. (1981). Bar instability and rotation curves. *A&A*, 99:362–374.
- Sellwood, J. A. (2013). *Dynamics of Disks and Warps*, page 923.
- Sellwood, J. A. and Wilkinson, A. (1993). Dynamics of barred galaxies. *Reports on Progress in Physics*, 56:173–256.
- Sharma, S., Johnston, K. V., Majewski, S. R., Muñoz, R. R., Carlberg, J. K., and Bullock, J. (2010). Group Finding in the Stellar Halo Using M-giants in the Two Micron All Sky Survey: An Extended View of the Pisces Overdensity? *ApJ*, 722:750–759.
- Sheffield, A. A., Price-Whelan, A. M., Tzanidakis, A., Johnston, K. V., Laporte, C. F. P., and Sesar, B. (2018). A Disk Origin for the Monoceros Ring and A13 Stellar Overdensities. *ApJ*, 854:47.
- Simmons, B. D., Melvin, T., Lintott, C., Masters, K. L., Willett, K. W., Keel, W. C., Smethurst, R. J., Cheung, E., Nichol, R. C., Schawinski, K., Rutkowski, M., Kartaltepe, J. S., Bell, E. F., Casteels, K. R. V., Conselice, C. J., Almaini, O., Ferguson, H. C., Fortson, L., Hartley, W., Kocevski, D., Koekemoer, A. M., McIntosh, D. H., Mortlock, A., Newman, J. A., Ownsworth, J., Bamford, S., Dahlen, T., Faber, S. M., Finkelstein, S. L., Fontana, A., Galametz, A., Grogin, N. A., Grützbauch, R., Guo, Y., Häußler, B., Jek, K. J., Kaviraj, S., Lucas, R. A., Peth, M., Salvato, M., Wiklind, T., and Wuyts, S. (2014). Galaxy Zoo: CANDELS barred discs and bar fractions. *MNRAS*, 445:3466–3474.

- Spitzer, Jr., L. (1942). The Dynamics of the Interstellar Medium. III. Galactic Distribution. *ApJ*, 95:329.
- Springel, V. (2005). The cosmological simulation code GADGET-2. *MNRAS*, 364:1105–1134.
- Tissera, P. B., Scannapieco, C., Beers, T. C., and Carollo, D. (2013). Stellar haloes of simulated Milky-Way-like galaxies: chemical and kinematic properties. *MNRAS*, 432:3391–3400.
- Toomre, A. (1964). On the gravitational stability of a disk of stars. *ApJ*, 139:1217–1238.
- Vasiliev, E. (2018). AGAMA: Action-based galaxy modelling architecture. *ArXiv e-prints*.
- Vogelsberger, M., Genel, S., Sijacki, D., Torrey, P., Springel, V., and Hernquist, L. (2013). A model for cosmological simulations of galaxy formation physics. *MNRAS*, 436:3031–3067.
- Widrow, L. M., Pym, B., and Dubinski, J. (2008). Dynamical Blueprints for Galaxies. *ApJ*, 679:1239–1259.
- Yanny, B., Newberg, H. J., Kent, S., Laurent-Muehleisen, S. A., Pier, J. R., Richards, G. T., Stoughton, C., Anderson, Jr., J. E., Annis, J., Brinkmann, J., Chen, B., Csabai, I., Doi, M., Fukugita, M., Hennessy, G. S., Ivezić, Ž., Knapp, G. R., Lupton, R., Munn, J. A., Nash, T., Rockosi, C. M., Schneider, D. P., Smith, J. A., and York, D. G. (2000). Identification of A-colored Stars and Structure in the



- Halo of the Milky Way from Sloan Digital Sky Survey Commissioning Data. *ApJ*, 540:825–841.
- Yurin, D. and Springel, V. (2015). The stability of stellar discs in Milky Way-sized dark matter haloes. *MNRAS*, 452:2367–2387.
- Zang, T. A. and Hohl, F. (1978). Computer experiments on the effect of retrograde stars in disk galaxies. *ApJ*, 226:521–539.

## Chapter 5

### Summary and Conclusions

#### 5.1 Summary

#### 5.2 Future Work

#### 5.3 Conclusion

## Appendix A

### Euler's Equations in Comoving Coordinates

The time-evolution of the angular momentum vector  $\mathbf{L}$  of a rigid body acted upon by a torque  $\boldsymbol{\tau}$  is given by

$$\left(\frac{d\mathbf{L}}{dt}\right)_f = \left(\frac{d\mathbf{L}}{dt}\right)_b + \boldsymbol{\omega} \times \mathbf{L} = \boldsymbol{\tau} \quad (\text{A.1})$$

where the subscripts  $f$  and  $b$  denote the frame of the simulation box and the body frame, respectively. In physical coordinates,  $\mathbf{L} = \mathbf{r} \times \mathbf{p}$ . Alternatively, we can write  $\mathbf{L} = \mathbf{s} \times \mathbf{q}$  where  $\mathbf{s} = a^{-1}\mathbf{r}$  refer to comoving coordinates and  $\mathbf{q} = a^2\dot{\mathbf{s}}$  is the conjugate momentum to  $\mathbf{s}$  (see ?).

For a rigid body, the components of the angular momentum are given by  $L_i = I_{ij}\omega_j$  where  $i, j$  run over  $x, y, z$  and there is an implied sum over  $j$ . Since GADGET-3 uses comoving coordinates, we write  $I_{ij} = a^2 J_{ij}$  where  $J$  is the moment of inertia tensor written in terms of the comoving coordinates,  $\mathbf{s}$ , rather than the physical coordinates,  $\mathbf{r}$ . For convenience, we define a “comoving” angular velocity  $\boldsymbol{\varpi} = a^{-2}\boldsymbol{\omega}$ . We then have  $L_i = J_{ij}\varpi_j$ . Note that because of the symmetry of our disc, the moment of inertia tensor is diagonal with  $J_{xx} = J_{yy} = J_{zz} \equiv J/2$ . The equations of motion for

the Euler angles and the disc angular velocity are then given by the standard Euler equations of rigid body dynamics, modified to account for the time-dependence of the disc's moment of inertia:

$$\frac{d\phi}{dt} = a^{-2} \sin^{-1} \theta (\varpi_x \sin(\psi) + \varpi_y \cos(\psi)) , \quad (\text{A.2})$$

$$\frac{d\theta}{dt} = a^{-2} (\varpi_1 \cos(\psi) - \varpi_y \sin(\psi)) , \quad (\text{A.3})$$

$$J \frac{\varpi_x}{dt} + \varpi_x \frac{dJ}{dt} + J \varpi_y \varpi_z = \tau_x , \quad (\text{A.4})$$

and

$$\frac{\varpi_y}{dt} + \varpi_y \frac{dJ}{dt} - J \varpi_x \varpi_z = \tau_y . \quad (\text{A.5})$$

We have omitted the equations for  $\psi$  (rotations in the body frame about the symmetry axis) and  $\varpi_z$  since these are determined directly from Eq. 3.8.